Quantitative real-time PCR. Primers and probe sets for the human *DNM2*, β-actin, and *GAPDH* genes were purchased from TaqMan Gene Expression Assay products (Applied Biosystems), and quantitative real-time PCR was carried out in an ABI PRISM 7900HT (Applied Biosystems). All quantitative PCRs were duplicated and the ratio of the amount of *DNM2* cDNA to that of β-actin or *GAPDH* internal control cDNA was determined at the cycle threshold (CT).

Cell culture. SH-SY5Y human neuroblastoma cells were stably transfected with Swedish mutant APP670/671(SY5Y/swAPP). Dominant negative pcDNA/dynamin 1K44A (*DNM1K44A*) and pcDNA/dynamin 2K44A (*DNM2K44A*) plasmids were obtained from ATCC. Transient transfections with DNM1K44A, DNM2K44A, or both in SY5Y/swAPP cells were performed using the Amaxa nucleofector system. To check viabilities of transfected cells, lactate dehydrogenase (LDH) levels were measured using an LDH kit (Promega).

Levels of Aβ40 and Aβ42. Culture media of SY5Y/swAPP cells were collected 72 h after transfection with dominant negative *DNM* plasmids. Using a human Aβ 1–40 ELISA kit and a human Aβ 1–42 ELISA kit (Biosource), the levels of Aβ 1–40 and Aβ 1–42 in culture media were quantified.

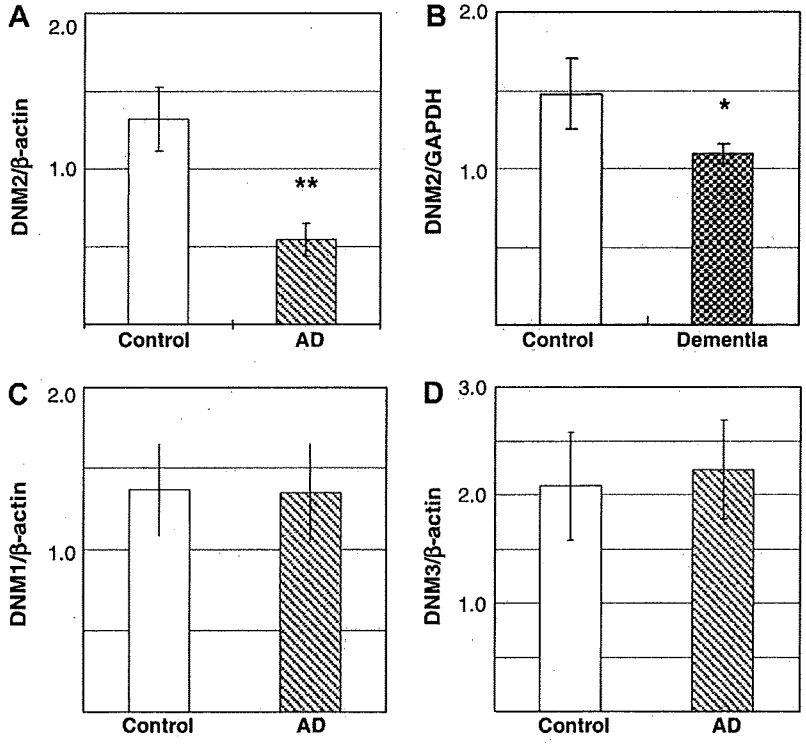

Fig. 1. Expression of *DNM* mRNA in the temporal cortex and in peripheral blood. Real-time PCR for *DNM2* (A), *DNM1* (C), and *DNM3* (D) mRNA from the temporal cortex of 7 AD and 7 control brains, normalized to β-actin mRNA, showed a significant reduction of *DNM2* mRNA levels in AD brains compared with control brains. In contrast, reduction of *DNM1* and *DNM3* levels were not observed. Analysis of *DNM2* mRNA, normalized to GAPDH mRNA, in peripheral leukocytes from 82 dementia patients and from 11 controls also revealed a significant reduction of *DNM2* mRNA (B). $^{*}p < 0.05$; $^{**}p < 0.01$.

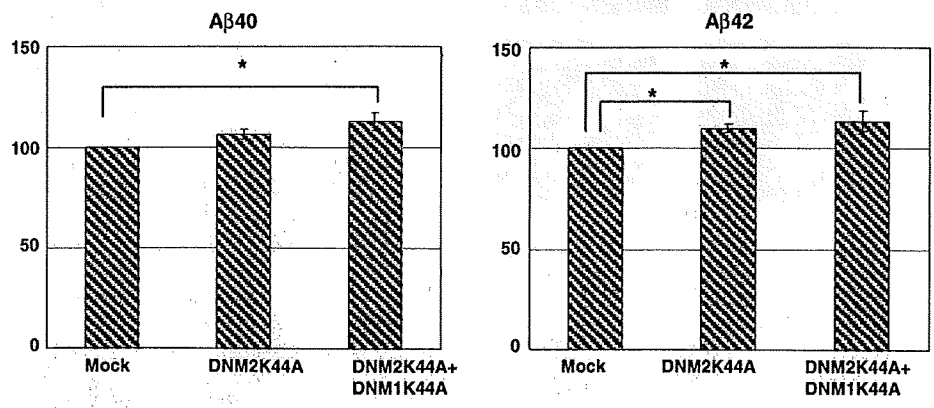

Fig. 2. Secretion of amyloid peptides (Aβ40 and Aβ42) in *DNM2* and *DNM1* dominant negative SY5Y/swAPP cells. ELISA of media 3 days after transfection showed that Aβ42 secretion was significantly increased in single *DNM2K44A* transfected cells and that both Aβ40 and Aβ42 secretion significantly increased in double *DNM2K44A* and *DNM1K44A* transfected cells. Levels of Aβ40 and Aβ42 in MOCK-transfected neuronal cells was combined. $^{*}p < 0.05$.

Sample preparation and Western blot analysis. Cell lysates were collected in PBS containing 2% Nonidet P-40, 0.2% SDS, protease inhibitor, and phosphatase inhibitor. Subcellular fractions of SY5Y/swAPP cells were collected using a ProteoExtract Subcellular Proteome Extraction Kit (Calbiochem). Biotinylated plasma membranes of SY5Y/swAPP cells were collected using a Cell Surface Protein Isolation Kit (Pierce). Equal amounts of each sample were separated by SDS–PAGE and electroblotted onto nitrocellulose membranes. Bands are visualized using a luminescent image analyzer Las-3000 and multi gauge software (Fujifilm).

Immunohistochemistry. SY5Y/swAPP cells transfected with dominant negative DNM were fixed in 4% paraformaldehyde, as described previously [6]. The samples were incubated with primary antibodies (see below) and then visualized with AlexaFluor568 goat anti-mouse IgG(H+L) (Invitrogen). APP staining and DAPI staining (Vector Laboratories) were examined using a Leica TCS SPE confocal microscope system (Leica Microsystems).

Antibodies. 22C11, APP monoclonal antibody, anti-presenilin 1 (Chemicon), Anti-flottillin-1 and anti-EEA1 (BD Transduction Laboratories), anti-pan-cadherin (Zymed Laboratories).

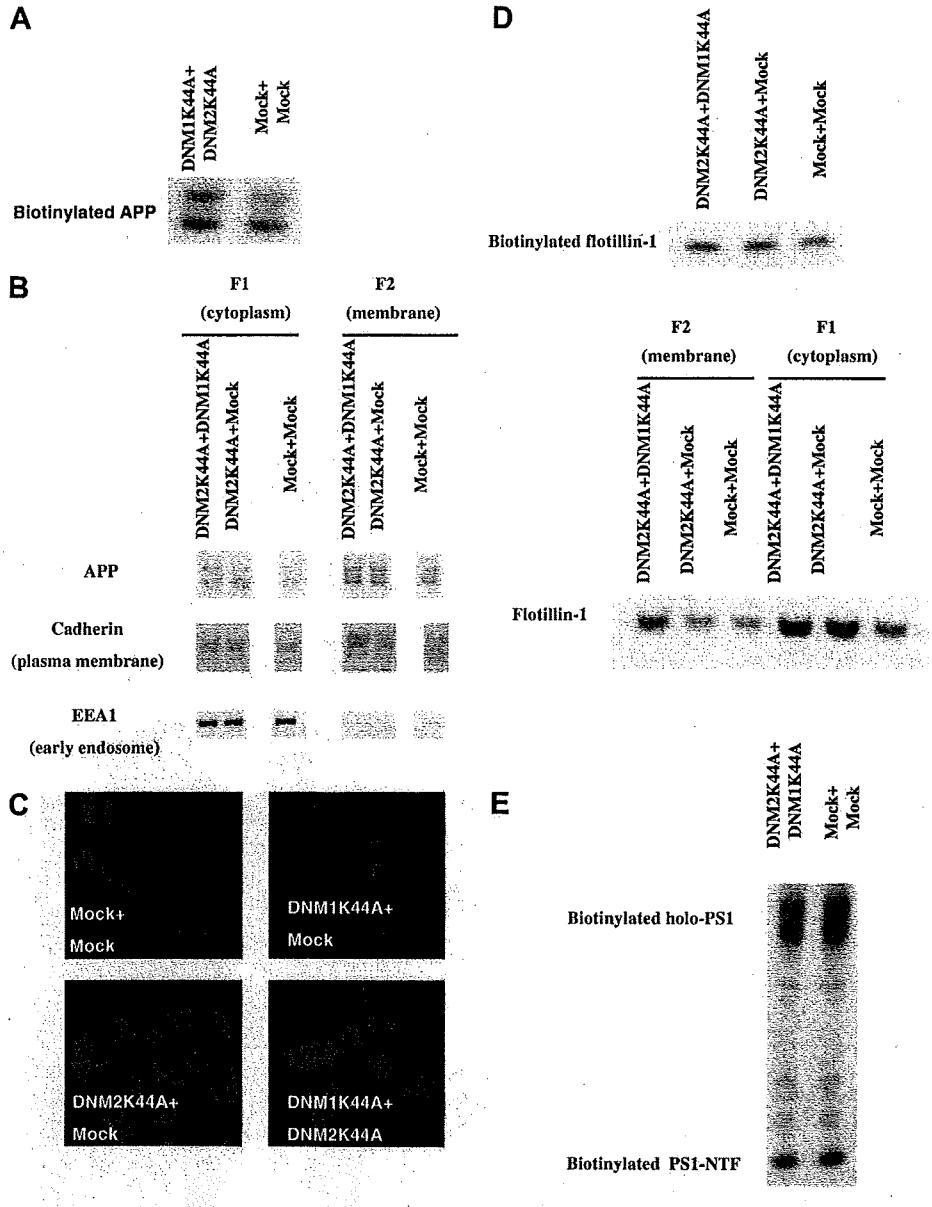

Fig. 3. Localization of APP, lipid raft, and PS1 in DNM dominant negative neuronal cells. (A) The cytoplasm and the membrane components of SY5Y/swAPP cells were fractionated using ProteoExtract Subcellular Proteome Extraction Kit, and each fraction was confirmed by immunoblotting with antibodies against specific marker proteins; cadherin for plasma membrane; EEA1 for early cytoplasmic endosome. Immunoblotting with anti-APP antibody showed that the membrane fraction of double *DNM2K44A* and *DNM1K44A* or of *DNM2K44A* transfected cells had increased amounts of APP, especially high molecular weight, mature APP. (B) Using a Cell Surface Protein Isolation Kit, the amount of biotinylated APP, especially high molecular weight, mature APP was increased in double *DNM2K44A* and *DNM1K44A* transfected cells compared with control. (C) Immunohistochemical examination showed that some APP staining (red) was observed on the cell surface of *DNM2K44A* transfected cells and of double transfected *DNM2K44A* and *DNM1K44A* cells, compared with MOCK-transfected cells. DAPI staining visualized nuclei in blue. (D) Using a Cell Surface Protein Isolation Kit, the amount of biotinylated flotillin-1, a marker for lipid raft, was shown to be increased in both single *DNM2K44A* transfected cells and in double *DNM2K44A* and *DNM1K44A* transfected cells. (E) Cell surface biotinylation showed that the plasma membrane of DNM dominant negative neuronal cells had enough amount of PS1-NTF and of holo-PS1 compared with MOCK-transfected cells. (For interpretation of the references in color in this figure legend, the reader is referred to the web version of this article.)

Results and discussion

To examine the expression of the *DNM* genes in the AD temporal cortex, we measured the amount of *DNM1*, *DNM2*, and *DNM3* mRNA, normalized to that of β-actin, using quantitative real-time PCR. Analysis of 7 AD tissues and 7 control tissues revealed that the amount of *DNM2* mRNA in the AD temporal cortex was significantly lower compared with that in controls (Fig. 1). On the other hand, the level of *DNM1* and *DNM3* mRNA in AD samples was not significantly different compared with that in controls (Fig. 1). Moreover, analysis of peripheral leukocytes from 82 dementia patients and from 11 controls revealed that the level of *DNM2* mRNA in dementia patients was significantly lower compared with that of controls (Fig. 1). These data suggest that *DNM2* may be one of the causal genes for LOAD. The dementia patients in the study of peripheral leukocytes consisted of patients with various forms of dementia, therefore, the analysis of *DNM2* mRNA in blood might be a biomarker for dementia.

It may be safely assumed that a decreased *DNM2* mRNA level causes dysfunction of DNM2. Because an increase of Aβ is the key event of AD pathology, we investigated the effects of DNM2 dysfunction on Aβ production using a neuronal cell line transfected with dominant negative *DNM* genes. We transiently transfected SY5Y/swAPP cells with either dominant negative *DNM2K44A or DNM1K44A*, or both. ELISA analysis of media 3 days after transfection showed that Aβ42 secretion significantly increased in *DNM2K44A* transfected cells and that both Aβ40 and Aβ42 secretion significantly increased in cells transfected with both *DNM2K44A* and *DNM1K44A* (Fig. 2). *DNM2K44A* transfected cells had a tendency of high Aβ40 levels, but the increase was not significant (Fig. 2). DNM1 has a similar structure to DNM2 [7], therefore, it was possible that DNM1 may compensate for DNM2 dysfunction in *DNM2K44A* cells. Therefore, it was suggested that the dysfunction of DNM2 may cause an increase of Aβ secretion.

A dominant negative DNM has been shown to cause an altered localization of amyloid precursor protein APP [8]. To elucidate the mechanism of increased Aβ production in the *DNM2* dominant negative neuronal cells, we focused on the localization of APP, 3 days after transfection. First, the cytoplasm and the membrane compartments of SY5Y/swAPP cells were fractionated, and each fraction was confirmed by immunoblotting with antibodies against specific marker proteins; cadherin for plasma membrane and EEA1 for cytoplasmic early endosomes [9,10]. Immunoblotting with anti-APP antibody showed that the membrane fraction of neuronal cells double transfected with *DNM2K44A* and *DNM1K44A* or singly transfected with *DNM2K44A* had increased amounts of APP, especially high molecular weight, mature APP (Fig. 3A). Because the membrane fraction contained high levels of cadherin, it mostly consisted of plasma membrane. Second we biotinylated the plasma membrane of SY5Y/swAPP cells using a Cell Surface Protein Isolation Kit. In neuronal cells double transfected with *DNM2K44A* and *DNM1K44A*, the amount of biotinylated APP, especially high molecular weight, mature APP, increased, suggesting that the amount of APP was increased in the plasma membrane of dominant negative neuronal cells (Fig. 3B). Third, immunohistochemical examination of SY5Y/swAPP cells was performed to investigate the localization of APP. In neuronal cells singly transfected with *DNM2K44A* and double transfected with *DNM2K44A* and *DNM1K44A*, higher levels of APP staining was observed on the cell surface compared with MOCK-transfected neuronal cells (Fig. 3C). Taken together, these data suggest that APP may accumulate in the plasma membrane in the *DNM2* dominant negative cells.

Recently, it has been reported that the lipid raft is a major location for Aβ generation [11–13]. Therefore, we examined the existence of lipid rafts in the plasma membrane of *DNM* dominant negative neuronal cells. The amount of biotinylated flotillin-1, a marker for lipid rafts, increased in both *DNM2K44A* transfected and *DNM2K44A* and *DNM1K44A* transfected neuronal cells suggesting that the amount of lipid raft was increased in the plasma membrane of *DNM2* dominant negative neuronal cells (Fig. 3D). This is consistent with recent reports of dominant negative *DNM* causing accumulation of lipid raft associated with invaginations of the plasma membrane [14,15]. We also examined the existence of presenilin 1 (PS1), a major component of the γ-secretase complex, in the plasma membrane of *DNM* dominant negative neuronal cells. Cell surface biotinylation showed that the plasma membrane of *DNM* dominant negative neuronal cells had enough amount of PS1-NTF and of holo-PS1 (Fig. 3E). These data suggest that Aβ generation may occur efficiently in the plasma membrane of *DNM* dominant negative neuronal cells.

APP is transported to the plasma membrane via the endoplasmic reticulum and the Golgi apparatus and is then taken up into endosomes by endocytosis [16], where Aβ generation occurs. In contrast, in neuronal cells that have lost DNM function APP accumulates in the plasma membrane. A major role of DNM is in vesicle endocytosis, and DNM function in vesicle budding is involved in the constriction of the lipid neck, fission of lipids and regulation of the scission reaction (for review, see [17]). According to our present data and to recent reports [13–15,18], lipid rafts or PS1 in the plasma membrane may be suitable locations for Aβ genera-

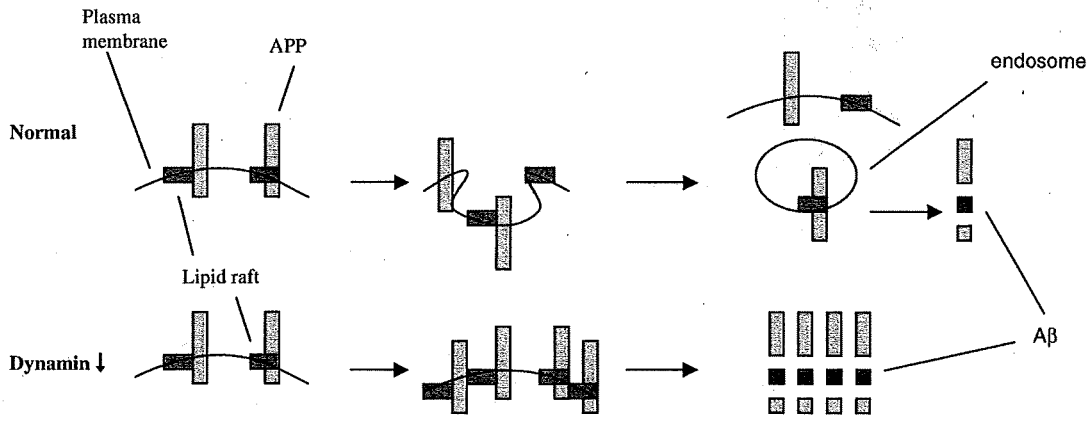

Fig. 4. Dysfunction of DNM2 increased Aβ generation as a result of the accumulation of APP in the plasma membrane. In normal conditions, APP is transported to plasma membrane through the endoplasmic reticulum and the Golgi apparatus and then is taken up in endosomes by endocytosis, where Aβ generation occurs. In contrast, neuronal cells that have lost DNM function may have an accumulation of APP in the plasma membrane, because the major role of DNM is in endocytosis. In DNM dominant negative neuronal cells increased Aβ production may occur due to the accumulation of APP and the presence of lipid raft or PS1 in the plasma membrane.

tion in *DNM* dominant negative neuronal cells, resulting in increased Aβ generation (Fig. 4).

Previously, we reported that SNP markers at the *DNM2* locus had a significant association with LOAD, especially in non-carriers of the apolipoprotein E-ε4 allele [4] The result of present study shows that *DNM2* mRNA levels were reduced in the temporal cortex and in peripheral blood. The relationship between the SNPs and the reduced level of *DNM2* message is not yet elucidated. However, this study showed that dysfunction of *DNM2* can cause an increase of Aβ generation that could be involved in amyloid pathology. The expression of *DNM2* and of *DNM1* is down-regulated by Aβ in hippocampal neurons [3]. Thus increased Aβ due to dysfunction of DNM2 may result in a positive feedback loop to further reduce DNM function. In conclusion, *DNM2* may be involved in Aβ pathology and may be a causal gene of LOAD.

References

[1] P.J. Yao, Synaptic frailty and clathrin-mediated synaptic vesicle trafficking in Alzheimer's disease, Trends Neurosci. 27 (2004) 24–29.

[2] D.J. Selkoe, Alzheimer's disease is a synaptic failure, Science 298 (2002) 789–791.

[3] B.L. Kelly, R. Vassar, A. Ferreira, β-Amyloid-induced dynamin 1 depletion in hippocampal neurons, J. Biol. Chem. 280 (2005) 31746–31753.

[4] N.J. Aidaralieva, K. Kamino, R. Kimura, M. Yamamoto, T. Morihara, H. Kazui, R. Hashimoto, T. Tanaka, T. Kudo, T. Kida, J. Okuda, T. Uema, H. Yamagata, T. Miki, H. Asatsu, K. Kosaka, M. Takeda, Dynamin 2 gene is a novel susceptibility gene for late-onset Alzheimer disease in non-APOE-ε4 carriers, J. Hum. Genet. 53 (2008) 296–302.

[5] R. Kuwano, A. Miyashita, H. Arai, T. Asada, M. Imagawa, M. Shoji, S. Higuchi, K. Urakami, A. Kakita, H. Takahashi, T. Tsukie, S. Toyabe, K. Akazawa, I. Kanazawa, Y. Ihara, The Japanese Genetic Study Consortium for Alzheimer's Disease, Dynamin-binding protein gene on chromosome 10q is associated with late-onset Alzheimer's disease, Hum. Mol. Genet. 15 (2006) 2170–2182.

[6] H. Ohno, S. Hirabayashi, T. Iizuka, H. Ohnishi, T. Fujita, Y. Hata, Localization of p0071-interacting proteins, plakophilin-related armadillo-repeat protein-interacting protein and ERBIN, in epithelial cells, Oncogene 21 (2002) 7042–7049.

[7] A.E. Kruchten, M.A. McNiven, Dynamin as a mover and pincher during cell migration and invasion, J. Cell. Sci. 119 (2006) 1683–1690.

[8] J.H. Chyung, D.J. Selkoe, Inhibition of receptor-mediated endocytosis demonstrates generation of amyloid β-protein at the cell surface, J. Biol. Chem. 278 (2003) 51035–51043.

[9] F.T. Mu, J.M. Callaghan, O. Steele-Mortimer, H. Stenmark, R.G. Parton, P.L. Campbell, J. McCluskey, J.P. Yeo, E.P. Tock, B.H. Toh, EEA1, an early endosome-associated protein. EEA1 is a conserved alpha-helical peripheral membrane protein flanked by cysteine "fingers" and contains a calmodulin-binding IQ motif, J. Biol. Chem. 270 (1995) 13503–13511.

[10] M. Takeichi, Cadherin cell adhesion receptors as a morphogenetic regulator, Science 251 (1991) 1451–1455.

[11] R. Ehehalt, P. Keller, C. Haass, C. Thiele, K. Simons, Amyloidogenic processing of the Alzheimer beta-amyloid precursor protein depends on lipid rafts, J. Cell. Biol. 160 (2003) 113–123.

[12] T. Kawarabayashi, M. Shoji, L.H. Younkin, L. Wen-Lang, D.W. Dickson, T. Murakami, E. Matsubara, K. Abe, K.H. Ashe, S.G. Younkin, Dimeric amyloid beta protein rapidly accumulates in lipid rafts followed by apolipoprotein E and phosphorylated tau accumulation in the Tg2576 mouse model of Alzheimer's disease, J. Neurosci. 24 (2004) 3801–3809.

[13] J.Y. Hur, H. Welander, H. Behbahani, M. Aoki, J. Frånberg, B. Winblad, S. Frykman, L.O. Tjernberg, Active gamma-secretase is localized to detergent-resistant membranes in human brain, FEBS J. 275 (2008) 1174–1187.

[14] I.R. Nabi, P.U. Le, Caveolae/raft-dependent endocytosis, J. Cell. Biol. 161 (2003) 673–677.

[15] P.U. Le, G. Guay, Y. Altschuler, I.R. Nabi, Caveolin-1 is a negative regulator of caveolae-mediated endocytosis to the endoplasmic reticulum, J. Biol. Chem. 277 (2002) 3371–3379.

[16] A. Schmitz, R. Tikkanen, G. Kirfel, V. Herzog, The biological role of the Alzheimer amyloid precursor protein in epithelial cells, Histochem. Cell Biol. 117 (2002) 171–180.

[17] G.J. Praefcke, H.T. McMahon, The dynamin superfamily: universal membrane tubulation and fission molecules?, Nat Rev. Mol. Cell. Biol. 5 (2004) 133–147.

[18] J.H. Chyung, D.M. Raper, D.J. Selkoe, Gamma-secretase exists on the plasma membrane as an intact complex that accepts substrates and effects intramembrane cleavage, J. Biol. Chem. 280 (2005) 4383–4392.

Biochemical and Biophysical Research Communications 383 (2009) 37–41

Contents lists available at ScienceDirect

Biochemical and Biophysical Research Communications

journal homepage: www.elsevier.com/locate/ybbrc

Differential interaction and aggregation of 3-repeat and 4-repeat tau isoforms with 14-3-3ζ protein

Golam Sadik, Toshihisa Tanaka *, Kiyoko Kato, Kentaro Yanagi, Takashi Kudo, Masatoshi Takeda

Department of Psychiatry, Graduate School of Medicine, Osaka University, D3, 2-2, Yamadaoka, Suita, Osaka 565-0871, Japan

ARTICLE INFO

Article history:
Received 18 March 2009
Available online 24 March 2009

Keywords:
Tau
14-3-3 protein
Phosphorylation
Alzheimer
Frontotemporal dementia

ABSTRACT

Tau isoforms, 3-repeat (3R) and 4-repeat tau (4R), are differentially involved in neuronal development and in several tauopathies. 14-3-3 protein binds to tau and 14-3-3/tau association has been found both in the development and in tauopathies. To understand the role of 14-3-3 in the differential regulation of tau isoforms, we have performed studies on the interaction and aggregation of 3R-tau and 4R-tau, either phosphorylated or unphosphorylated, with 14-3-3ζ. We show by surface plasmon resonance studies that the interaction between unphosphorylated 3R-tau and 14-3-3ζ is ~3-folds higher than that between unphosphorylated 4R-tau and 14-3-3ζ. Phosphorylation of tau by protein kinase A (PKA) increases the affinity of both 3R- and 4R-tau for 14-3-3ζ to a similar level. An *in vitro* aggregation assay employing both transmission electron microscopy and fluorescence spectroscopy revealed the aggregation of unphosphorylated 4R-tau to be significantly higher than that of unphosphorylated 3R-tau following the induction of 14-3-3ζ. The filaments formed from 3R- and 4R-tau were almost similar in morphology. In contrast, the aggregation of both 3R- and 4R-tau was reduced to a similar low level after phosphorylation with PKA. Taken together, these results suggest that 14-3-3ζ exhibits a similar role for tau isoforms after PKA-phosphorylation, but a differential role for unphosphorylated tau. The significant aggregation of 4R-tau by 14-3-3ζ suggests that 14-3-3 may act as an inducer in the generation of 4R-tau-predominant neurofibrillary tangles in tauopathies.

Introduction

In neurodegenerative diseases with dementia, like Alzheimer's disease (AD), abnormal accumulation of aggregative products, i.e., amyloid beta and tau protein, has been characterized thoroughly. However, the mechanisms of pathological processes are still unclear [1,2]. Tau is a microtubule-associated protein expressed predominantly in neurons, where its major known biological function is to stimulate microtubule (MT) assembly and to stabilize the MT network. Tau comprises a family of six isoforms generated by alternative mRNA splicing from a single gene [3,4]. They fall into two groups, one of which contains four C-terminal imperfect repeat domains and the other, three such repeat domains. Phosphorylation [5] and expression of the different isoforms [6] are two important mechanisms by which tau regulate microtubule polymerization and stabilization of microtubules during development. Whereas in the fetal brain, tau is phosphorylated at multiple sites and only 3R-tau is expressed, in adults tau is phosphorylated at only a few sites and both 3R- and 4R-tau are expressed in almost equal proportion. *In vitro* studies have shown that phosphorylated tau and 3R-tau isoforms bind and stabilize the microtubule more weakly than unphosphorylated tau and 4R-tau isoforms [7], thus indicating that the regulation of phosphorylation and expression of tau isoforms is required for microtubule dynamics during development. Despite its physiological role, tau is central to the pathogenesis of tauopathies as it becomes abnormally hyperphosphorylated and aggregated in these diseases. The predominant aggregation of either 3R- or 4R-tau is another characteristic to certain tauopathies [8]. For example, in Pick's disease (PiD) 3R tau is predominantly accumulated, but in progressive supranuclear palsy (PSP) and in frontotemporal dementia and parkinsonism linked to chromosome 17 (FTDP-17), accumulation of 4R-tau is predominant. Genetic mutations in tau alter the 3R/4R tau ratio in FTDP-17 due to splicing of exon 10 [6]. However, in other tauopathies such as PiD, PSP and corticobasal degeneration (CBD), where no mutations have been reported, the exact causes and mechanisms leading to the altered 3R-/4R-tau ratios remain elusive.

Tau is a very soluble protein and does not assemble readily *in vitro* even at high concentrations. Increasing the levels of tau in both animal and cell culture models through transgenic expression of wild-type human tau at concentrations that saturate the endogenous MT also failed to result in robust tau assembly [9]. However, cofactors, also called exogenous inducers, such as

* Corresponding author. Fax: +81 6 6879 3059.
E-mail address: tanaka@psy.med.osaka-u.ac.jp (T. Tanaka).

0006-291X/$ - see front matter © 2009 Elsevier Inc. All rights reserved.
doi:10.1016/j.bbrc.2009.03.107

heparin, RNA, glycosaminoglycans, etc. have been found associated with neurofibrillary tangles (NFTs) and promote the aggregation of tau independently of phosphorylation [10–12]. Therefore, it seems reasonable to consider that the assembly of tau to form inclusions *in vivo* also requires the presence of cofactors that might be specific in certain tauopathies and may differentially induce tau aggregation. The identification of such cofactors may provide new insights into the pathogenesis of tauopathy.

14-3-3 is a family of highly conserved abundant regulatory proteins found in all eukaryotes and involved in many intracellular processes such as cell cycle control, apoptosis, signal transduction cascades and cytoskeletal reorganization [13]. It is a phosphoprotein binding protein that generally binds to its partner in a phosphorylation dependent manner. Tau is a phosphoprotein and we have recently reported that 14-3-3ζ binds to tau regulated by phosphorylation of tau at Ser214 by PKA [14]. The binding is of high affinity which greatly reduces tau aggregation. Since tau is highly phosphorylated at Ser214 and its complex with 14-3-3ζ is found at greater levels in the fetal brain, the interaction of tau with 14-3-3 may underlie the reorganization of the microtubule cytoskeleton during development. Despite a possible role in development, 14-3-3 has been found to be associated with neurofibrillary tangles (NFTs) in several tauopathies, including AD, PiD [15–17], and able to interfere with the steps of tau pathology. It modulates phosphorylation of tau at sites that are hyperphosphorylated in AD [18] and promotes aggregation of tau into filaments by binding to its repeat domain independently of phosphorylation [19]. However, the role of 14-3-3 in normal and abnormal tau action is only incompletely understood.

As 3R- and 4R-tau isoforms are differentially involved in neuronal development and in tauopathies and as 14-3-3 proteins are found to be associated with tau in both of the physiological and pathological conditions, investigating the interaction and aggregation of tau isoforms with 14-3-3 may provide further understanding of the possible role of 14-3-3 in the physiological and pathological tau action.

Materials and methods

Antibodies and Western blotting. Tau-5 monoclonal antibody, which reacts equally with both the phosphorylated and nonphosphorylated tau, was purchased from BioSource International (Camarillo, CA, USA). CP-3 antibody, which recognizes phosphorylated Ser214 was a gift from Dr. Peter Davis (Albert Einstein University, New York, NY, USA). Western blotting was performed as previously described [14].

Protein kinases. The catalytic subunits of protein kinase A (PKA) were purchased from Sigma (Saint Louis, MI, USA). One unit of PKA was defined as the amount of enzyme which catalyzed the incorporation of 1 pmol of phosphate into the synthetic peptide LRRASLG in 1 min.

Recombinant proteins. Recombinant 14-3-3ζ was prepared following the method described earlier [18]. Human tau with 3- or 4-repeats (411- or 441-residue isoforms, Fig. 1) were subcloned into pET-22b for bacterial expression and transformed into *E. coli* BL21 (DE3) for expression of the histidine-tagged protein. The protein was purified as described previously [14] and purity was assessed on sodium dodecyl sulphate–polyacrylamide gel (SDS–PAGE, 10%) stained with Coomassie brilliant blue (CBB).

In vitro phosphorylation of tau. Phosphorylation was carried out by incubating tau (0.2 mg/ml) at 30 °C for 6 h in a reaction mixture containing 50 mM Tris–HCl (pH 7.4), 1 mM DTT, 10 mM $MgCl_2$, and

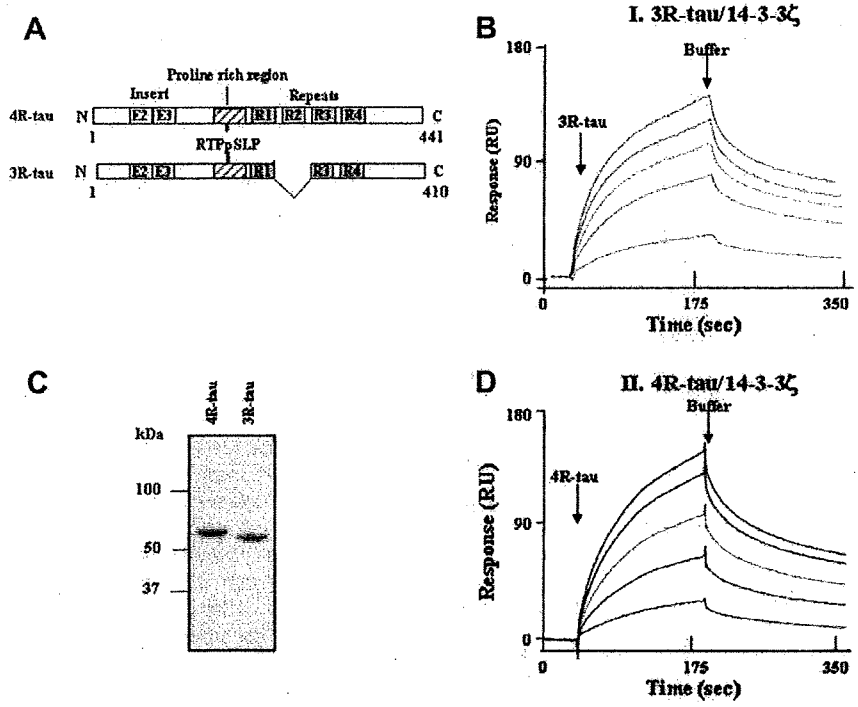

Fig. 1. 14-3-3ζ binds to unphosphorylated 3R-tau with higher affinity than unphosphorylated 4R-tau. (A) A schematic diagram of the longest human 4R- and 3R-tau isoforms employed. The amino acid residues numbers are according to tau441. 4R-tau contains two alternatively spliced inserts near the N-terminus (E2 and E3) and 4-repeats (~31 residues each, R1–R4) in the C-terminal half. 3R-tau differs from 4R-tau only by the absence of R2, due to alternative splicing of exon 10. The positions of the phosphorylation-dependent binding motif of 14-3-3, 211-RTPpSLP-216 in 4R- and 3R-tau, are highlighted. (B) CBB-stained SDS–polyacrylamide gel (10%) of purified recombinant 4R- and 3R-tau proteins. (C) Overlay of SPR sensograms resulting from the injection of 50, 100, 150, 200, and 250 nM (from bottom to top) unphosphorylated tau over immobilized 14-3-3ζ. I, 3R-tau; II, 4R-tau. The arrows represented by 3R- or 4R-tau and buffer indicated the start of the association and dissociation curves, respectively.

Table 1
Kinetic constants for the interaction between tau and 14-3-3ζ obtained by SPR.

	k_a (M^{-1} s^{-1})	k_d (s^{-1})	K_A (M^{-1})	K_D (M)
4R-tau	$3.66 \pm 0.17 \times 10^3$	$1.17 \pm 0.16 \times 10^{-3}$	$3.07 \pm 0.32 \times 10^6$	$3.25 \pm 0.44 \times 10^{-7}$
3R-tau	$2.40 \pm 0.38 \times 10^4$	$2.68 \pm 0.33 \times 10^{-3}$	$0.90 \pm 0.06 \times 10^7$	$1.13 \pm 0.06 \times 10^{-7}$
PKA-phospho 4R-tau	$6.27 \pm 0.30 \times 10^4$	$1.93 \pm 0.28 \times 10^{-3}$	$3.30 \pm 0.61 \times 10^7$	$2.91 \pm 0.61 \times 10^{-8}$
PKA-phospho 3R-tau	$5.86 \pm 0.08 \times 10^4$	$1.26 \pm 0.16 \times 10^{-3}$	$4.63 \pm 0.34 \times 10^7$	$2.16 \pm 0.34 \times 10^{-8}$

2 mM ATP with 100 U/ml of PKA. The reactions were stopped by boiling for 5 min and heat stable tau protein was removed from the denatured kinases by centrifugation (10,000*g* for 10 min).

Surface plasmon resonance (SPR) studies of 14-3-3ζ and tau. The affinity of unphosphorylated or phosphorylated tau with 14-3-3ζ was measured by surface plasmon resonance (SPR) spectroscopy using a Biacore 2000 (Biacore, Inc., Uppsala, Sweden) as described [14]. In brief, 14-3-3ζ was immobilized to the desired level on one flow cell (FC2) of a CM5 sensor chip by primary amine coupling, according to the manufacturer's instructions. A blank surface (FC1) was made by ethanolamine deactivation of the activated dextran surface. Purified tau, unphosphorylated tau or phosphorylated, at various concentrations (50–250 nM) was injected over the flow cells (FC1 and FC2) at a rate of 40 μl/min and the bound analytes were removed by washing with buffer after the injection. The first flow cell (FC1) was the minus tau protein control channel and was subtracted from the sample channel (FC2) during the run. The bulk refractive index contributions were therefore expected to be zero or not significant in the reference subtracted sensograms. To correct for nonspecific binding, blank runs were performed with HBS-EP buffer on both surfaces before and after each binding analysis and this value was subtracted prior to the kinetic analysis. Equilibrium association and dissociation rate constants were calculated using the Langmuir (1:1) binding model with the BIA evaluation 2.1 software supplied by the manufacturer.

In vitro aggregation and fluorescence spectroscopy. Aggregation was induced by incubating tau at a concentration of 20 μM in 50 mM Tris–HCl (pH 7.4) buffer, 150 mM NaCl and 4 mM DTT at 37 °C for different time periods, and mixing it with 14-3-3ζ in an equimolar ratio. At each time point, the aggregation of tau was monitored by measuring the fluorescence of Thioflavine S (ThS) using a spectrofluorometer (Perkin-Elmer Japan, Kanagawa, Japan) with an excitation filter of 430 nm and an emission filter of 520 nm. Measurements were carried out at room temperature in Tris–HCl buffer with 10 μM ThS and typically done in triplicate. Background fluorescence and light scattering of the sample without ThS was subtracted when needed. Curves show average values.

Electron microscopy. Polymerization samples were applied to a 300 mesh carbon-coated grid and negatively stained with 2% (w/v) uranyl acetate as described earlier [14]. Grids were analyzed using a JEOL JEM-1220 EM instrument at 50 kV.

Results and discussion

Alternative splicing of exon 10 gives rise to two major types of tau isoforms, 3R- and 4R-tau that differ by the absence or presence of the R2 repeat, respectively [6]. They show key differences in binding with their partners as well as their biological functions. 14-3-3 binds to the repeat domain of tau independently of phosphorylation [14,18]; however, the extent of binding with the different tau isoforms is unknown. To determine whether 14-3-3 exhibits any differences in interaction with tau isoforms independently of phosphorylation, we used the 4R- and 3R-tau with full N-terminal insertions (Fig. 1) and assessed their interaction with 14-3-3ζ by surface plasmon resonance (SPR) spectroscopy, using a Biacore 2000 as described earlier [14]. Real time interaction between unphosphorylated tau and 14-3-3ζ was measured at 25 °C by injecting tau onto a sensor chip with immobilized 14-3-3ζ.

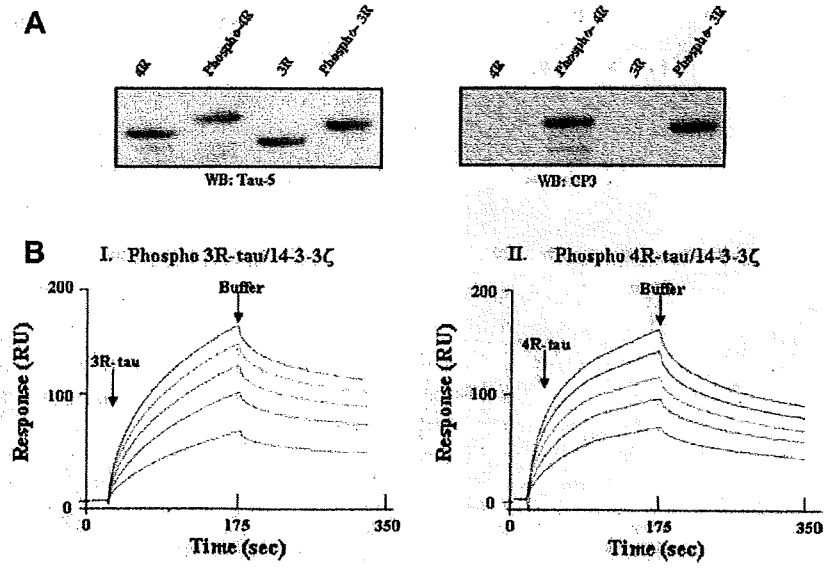

Fig. 2. 14-3-3ζ shows almost equal affinity for phosphorylated 3R- and 4R-tau. (A) Tau was phosphorylated with PKA and the phosphorylation sites were analyzed by Western blotting with the indicated phosphorylation-independent and -dependent antibodies. B, An overlay of SPR sensograms resulting from the injection of 50, 100, 150, 200, and 250 nM (from bottom to top) tau over immobilized 14-3-3ζ. I, PKA-phosphorylated 3R-tau; II, PKA-phosphorylated 4R-tau. The arrows represented by 3R- or 4R-tau and buffer indicated the start of the association and dissociation curves, respectively.

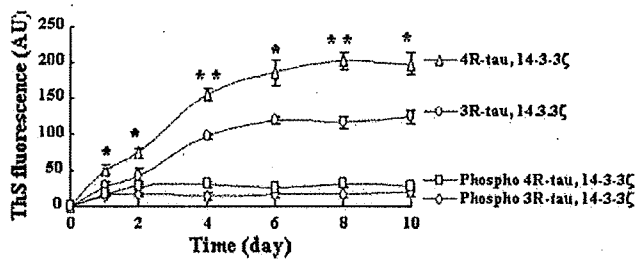

Fig. 3. Unphosphorylated 4R-tau is assembled more readily than unphosphorylated 3R-tau by the induction of 14-3-3ζ in vitro. The rate of aggregation of unphosphorylated 4R-tau (△) and 3R-tau (○) or phosphorylated 4R-tau (□) and 3R-tau (◇) were measured by ThS fluorescence. The intensity of ThS (AU) is plotted as a function of induction time. The values are means ± SD, $n = 3$, from a single microplate. $^{*}P < 0.05$, $^{**}P < 0.01$ when compared with 3R-tau. Data were analyzed by Student's t-test.

The binding of 14-3-3ζ to tau caused an increase in mass at the surface of the chip which was reflected by an increase in SPR response over time (Fig. 1). Different concentrations of tau ranging from 50 to 250 nM were used to quantitatively determine the association and dissociation constants (Table 1). The equilibrium dissociation constant (K_D) for the interaction of unphosphorylated 3R-tau with 14-3-3ζ was ~113 nM, whereas the K_D between 14-3-3ζ and unphosphorylated 4R-tau was 325 nM. Approximately 3-folds more affinity was observed between 3R-tau and 14-3-3ζ in comparison to 4R-tau, which suggests that the R2 domain has an impact on the affinity of 4R-tau with 14-3-3ζ. The differences in interaction between 3R- and 4R-tau could be caused by isoform specific folding as suggested from earlier studies with microtubules [7]. These results are consistent with the reported evidence that Src family nonreceptor tyrosine kinases, fyn and Src, interact with 3R-tau at higher affinity than 4R-tau [20]. The impact of the R2 repeat is apparent, even though fyn and Src interact with tau at the proline rich domain which is close to the N-terminus of repeats.

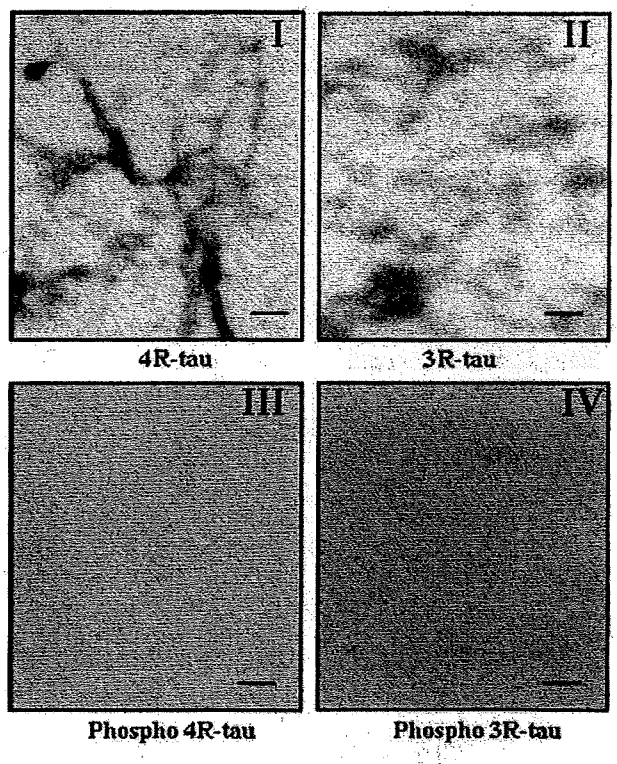

Fig. 4. Negative stain electron micrographs of filaments of 3R- and 4R-tau. Filaments of unphosphorylated 4R-tau (I) and 3R-tau (II) or phosphorylated 4R-tau (III) and 3R-tau (IV) assembled in the presence of 14-3-3ζ (same filament preparations as for the kinetic data at the endpoint of assembly). The size bar for 3R- and 4R-tau represent 330 and 500 nm, respectively.

Our previous study demonstrated that 14-3-3ζ binds to tau with higher affinity when tau is phosphorylated by PKA at Ser214 [14]. The primary structure of 4R-tau at Ser214 (209-RSRTPpSLP-216) is very similar to the canonical binding motif of 14-3-3 (RS/TXpSXP) [13]). In 3R-tau, Ser214 as well as the residues that compose the motif are conserved. To determine whether 14-3-3ζ exhibits any differences in interaction between 3R- and 4R-tau mediated by phosphorylation, the interaction was measured by SPR after phosphorylating tau at Ser214. 3R- and 4R-tau were phosphorylated by incubating them with PKA in a reaction mixture described earlier [14] and phosphorylation of tau at Ser214 was confirmed by immunoblotting with phosphorylated-Ser214 dependent CP3 antibody (Fig. 2A). The K_D values for the interaction of 3R- and 4R-tau with 14-3-3ζ were estimated to be 21 and 29 nM, respectively (Fig. 2B, and Table 1), thus suggesting that 14-3-3ζ has almost similar affinity for both 3R- or 4R-tau when tau is phosphorylated at Ser214. These results indicate that phosphorylation at Ser214, which is conserved in all the isoforms, might induce a drastic change in the conformation of tau such that 14-3-3 displays a similar strong affinity for both the isoforms. Recently, Sluchanko et al. [21] reported the interaction between 14-3-3ζ and the smallest 3R-tau isoform with or without phosphorylation. Our results are in accordance with their conclusion that phosphorylation of 3R-tau by PKA increases its interaction with 14-3-3ζ, but differ in the equilibrium dissociation constant, presumably due to experimental procedures, such as the method of determining the constants or the state of phosphorylation and oligomerization of tau that also might affect the tau/14-3-3 interaction.

14-3-3ζ facilitates tau aggregation by binding to its repeat domain [14,19]. Since 14-3-3ζ displays a higher affinity for 3R-tau than for 4R-tau, aggregation of both 3R- and 4R-tau was examined in the presence of 14-3-3ζ using the ThS fluorescence method. Equimolar amounts of 3R- and 4R-tau were incubated with 14-3-3ζ and the rate of aggregation was monitored by measuring samples at different time periods. The results (Fig. 3) show a significant increase in the aggregation of 4R-tau compared to 3R-tau under the same conditions. Tau aggregates were checked for filaments by negative stain electron microscopy (EM) and the results were very consistent with the results from ThS fluorescence assay. 4R-tau produced more filaments than 3R-tau (Fig. 4), but most filaments from both 4R- and 3R-tau were long and straight, thus suggesting that the aggregation was based on similar structural principles.

Phosphorylation of tau at Ser214 by PKA has been shown earlier to drastically reduce the aggregation of tau following the induction by 14-3-3ζ [14]. To determine the difference in aggregation between phosphorylated 3R- and 4R-tau, tau was phosphorylated by PKA at Ser214 and aggregation of phosphorylated tau was measured by ThS fluorescence method after incubation with 14-3-3ζ. Results (Fig. 3) showed that both 4R- and 3R-tau isoforms aggregated to a similar low level, suggesting that phosphorylation reduces the aggregation of both tau isoforms presumably in a similar manner. The results of ThS fluorescence studies were confirmed by negative stain electron microscopy (EM) and no filaments were found (Fig. 4).

Our results demonstrate that 14-3-3ζ binds to and induce the assembly of 3R- and 4R-tau isoforms differentially when tau is unphosphorylated, but similarly when tau is phosphorylated at Ser214 by PKA. Although the differential affinity of 3R- and

4R-tau for 14-3-3ζ is consistent with their differential aggregation by induction of 14-3-3ζ, the high affinity of 3R-tau relative to 4R-tau but the weak aggregation of 3R-tau than 4R-tau tempts us to speculate that like arachidonic acid- or heparin-induced aggregation of tau, the binding of 14-3-3ζ to tau is probably an obligate step preceding tau-tau interaction for aggregation [12,22]. The assembly behavior of 3R- and 4R-tau isoforms by induction of 14-3-3ζ appears to be very similar to the polyanion inducer heparin or fatty acid inducer arachidonic acid, which induces more aggregation of 4R-tau than 3R-tau [12,22–23]. In contrast, the similar level of high affinity and low aggregation of 3R- and 4R-tau isoforms after phosphorylation at Ser214 by PKA suggest that upon Ser214 phosphorylation, both isoforms might adopt a similar conformation for which they show similar higher affinity for 14-3-3ζ and resist aggregation to a similar extent by induction of 14-3-3ζ. Altogether, these results showed that 14-3-3ζ exhibits a similar role for tau isoforms in phosphorylated form, but a differential role in unphosphorylated form, which might have significance in tauopathy.

Tauopathies are mostly sporadic, and it is possible that different cofactors may function to induce the differential aggregation of tau isoforms that accumulate in inclusions observed in AD, PSP, CBD, and PiD. Some inducers may be effective in promoting the assembly of any tau isoforms, whereas others may prefer 4R- or 3R-tau. In this regard, *in vitro* studies have shown that tau isoforms can be differentially aggregated by cofactors other than 14-3-3, such as heparin, arachidonic acid, RNA. However, their involvement in the formation of NFT *in vivo* remains debated. For example, heparin is primarily extracellular, whereas tau protein is exclusively intracellular. Similarly, RNA is intracellular and present at high concentration, but is heavily complexed with proteins and not clear of its availability in free form in a sufficient amount to induce tau filament formation. The level of free cytoplasmic arachidonic acid is quiet low in the normal brain, whereas a high concentration of arachidonic acid is required for tau polymerization [24]. In comparison with the cofactors identified to date, 14-3-3 appears to be a potential candidate in the generation of NFTs in tauopathies for several reasons: first, 14-3-3 is an abundant cytosolic protein, which accounts for more than 1% of the total soluble protein. Second, 14-3-3 is a natural partner of tau and it facilitates tau aggregation by binding to its repeat domain, and third, 4R-tau is more aggregated than 3R-tau in presence of 14-3-3ζ. The observation of preferential interaction of 14-3-3ζ with 3R-tau than with 4R-tau, and induction of predominant aggregation of 4R-tau in comparison with 3R-tau may explain the association of 14-3-3 with NFTs found in tauopathies [15–17,25]. Therefore, 14-3-3 is probably the most important cofactor, identified to date, involved in the generation of NFTs predominantly of 4R-tau and our study will certainly be valuable in future research to clarify the role of 14-3-3 as a physiological inducer *in vivo*.

Acknowledgments

This work was, in part, supported by Grants from the Ministry of Education, Culture, Sports, Science, and Technology of Japan (No. 18591286 and No. 19390305). We feel grateful for the 14-3-3 cDNA provided by T. Ichimura of Tokyo Metropolitan University, Japan and for CP3 antibody provided by P. Davies of Albert Einstein University, New York, NY, USA.

References

[1] T. Kudo, H. Tanii, M. Takeda, Neurodegenerative dementias involving aberrant protein aggregation, Psychogeriatrics 7 (2007) 114–117.
[2] T. Tanaka, M. Tomioka, G. Sadik, M. Takeda, 13th Congress of the International Psychogeriatric Association and recent expansion of research into psychogeriatrics, Psychogeriatrics 7 (2007) 1–3.
[3] A. Himmler, D. Drechsel, M.W. Kirschner, D.W.J. Martin, Tau consists of a set of proteins with repeated C-terminal microtubule-binding domains and variable N-terminal domains, Mol. Cell. Biol. 9 (1989) 1381–1388.
[4] M. Goedert, M.G. Spillantini, R. Jakes, D. Rutherford, R.A. Crowther, Multiple isoforms of human microtubule-associated protein tau: sequences and localization in neurofibrillary tangles of Alzheimer's disease, Neuron 3 (1989) 519–526.
[5] G.V. Johnson, W. Stoothoff, Tau phosphorylation in neuronal cell function and dysfunction, J. Cell Sci. 117 (2004) 5721–5729.
[6] A. Andreadis, Tau gene alternative splicing: expression patterns, regulation and modulation of function in normal brain and neurodegenerative diseases, Biochim. Biophys. Acta 1739 (2005) 91–103.
[7] B.L. Goode, M. Chau, P.E. Denis, S.C. Feinstein, Structural and functional differences between 3-repeat and 4-repeat tau isoforms. Implications for normal tau function and the onset of neurodegenerative disease, J. Biol. Chem. 275 (2000) 38182–38189.
[8] K. Iqbal, A.delC. Alonso, S. Chen, M.O. Chohan, E. El-Akkad, C.-X. Gong, S. Khatoon, B. Li, F. Liu, A. Rahman, H. Tanimukai, I. Grundke-Iqbal, Tau pathology in Alzheimer disease and other tauopathies, Biochim. Biophys. Acta 1739 (2005) 198–210.
[9] L.-W. Ko, T. Rush, N. Sahara, J.S. Kersh, C. Easson, M. Deture, W.-L. Lin, Y.D. Connor, S.-H. Yen, Assembly of filamentous tau aggregates in human neuronal cells, J. Alz. Dis. 6 (2004) 605–622.
[10] T. Kampers, P. Friedhoff, J. Biernat, E.-M. Mandelkow, E. Mandelkow, RNA stimulates aggregation of microtubule-associated protein tau into Alzheimer-like paired helical filaments, FEBS Lett. 399 (1996) 344–349.
[11] M. Hasegawa, R.A. Crowther, R. Jakes, M. Goedert, Alzheimer-like changes in microtubule-associated protein Tau induced by sulfated glycosaminoglycans. Inhibition of microtubule binding, stimulation of phosphorylation, and filament assembly depend on the degree of sulfation, J. Biol. Chem. 272 (1997) 33118–33124.
[12] M.E. King, V. Ahuja, L.I. Binder, J. Kuret, Ligand-dependent tau filament formation: Implications for Alzheimer's disease progression, Biochemistry 38 (1999) 14851–14859.
[13] D. Berg, C. Holzman, O. Riess, 14-3-3 proteins in the nervous system, Nat. Rev. Neurosci. 4 (2003) 752–762.
[14] G. Sadik, T. Tanaka, K. Kato, H. Yamamori, B.N. Nessa, T. Morihara, M. Takeda, Phosphorylation of tau at Ser214 mediates its interaction with 14-3-3 protein: implications for the mechanism of tau aggregation, J. Neurochem. 108 (2009) 33–43.
[15] R. Layfield, J. Fergusson, A. Aitken, J. Lowe, M. Landon, R.J. Mayer, Neurofibrillary tangles of Alzheimer's disease brains contain 14-3-3 proteins, Neurosci. Lett. 209 (1996) 57–60.
[16] T. Umahara, T. Uchihara, K. Tsuchiya, A. Nakamura, T. Iwamoto, K. Ikeda, M. Takasaki, 14-3-3 proteins and zeta isoform containing neurofibrillary tangles in patients with Alzheimer's disease, Acta Neuropathol. (Berl) 108 (2004) 279–286.
[17] T. Umahara, T. Uchihara, K. Tsuchiya, A. Nakamura, K. Ikeda, T. Iwamoto, M. Takasaki, Immunolocalization of 14-3-3 isoforms in brains with Pick body disease, Neurosci. Lett. 371 (2004) 215–219.
[18] M. Hashiguchi, K. Sobue, H.K. Paudel, 14-3-3 zeta is an effector of tau protein phosphorylation, J. Biol. Chem. 275 (2000) 25247–25254.
[19] F. Hernandez, R. Cuadors, J. Avila, Zeta 14-3-3 protein favours the formation of human tau fibrillar polymers, Neurosci. Lett. 357 (2004) 143–146.
[20] K. Bhaskar, S.H. Yen, G. Lee, Disease-related modifications in tau affect the interaction between Fyn and Tau, J. Biol. Chem. 280 (2005) 35119–35125.
[21] N.N. Sluchanko, A.S. Seit-Nebi, N.B. Gusev, Effect of phosphorylation on interaction of human tau protein with 14-3-3ζ, Biochem. Biophys. Res. Commun. 379 (2009) 990–994.
[22] S. Jeganathan, M. von Bergen, E.-M. Mandelkow, E. Mandelkow, The natively character of tau and its aggregation to Alzheimer-like paired helical filament, Biochemistry 47 (2008) 10526–10539.
[23] N. Sahara, S. Maeda, M. Murayama, T. Suzuki, N. Dohmae, S.H. Yen, A. Takashima, Assembly of two distinct dimers and higher-order oligomers from full-length tau, Eur. J. Neurosci. 25 (2007) 3020–3029.
[24] M.E. King, T.C. Gamblin, J. Kuret, L.I. Binder, Differential assembly of human tau isoforms in the presence of arachidonic acid, J. Neurochem. 74 (2000) 1749–1757.
[25] K. Sugimori, K. Kobayashi, T. Kitamura, S. Sudo, Y. Koshino, 14-3-3 protein beta isoform is associated with 3-repeat tau neurofibrillary tangles in Alzheimer's disease, Psychiatry Clin. Neurosci. 61 (2007) 159–167.

Effect of an Inducer of BiP, a Molecular Chaperone, on Endoplasmic Reticulum (ER) Stress-Induced Retinal Cell Death

Yuta Inokuchi,[1] *Yoshimi Nakajima,*[1] *Masamitsu Shimazawa,*[1] *Takanori Kurita,*[2] *Mikiko Kubo,*[3] *Atsushi Saito,*[4] *Hironao Sajiki,*[2] *Takashi Kudo,*[3] *Makoto Aihara,*[5] *Kazunori Imaizumi,*[4] *Makoto Araie,*[5] *and Hideaki Hara*[1]

Purpose. The effect of a preferential inducer of 78 kDa glucose-regulated protein (GRP78)/immunoglobulin heavy-chain binding protein (BiP; BiP inducer X, BIX) against tunicamycin-induced cell death in RGC-5 (a rat ganglion cell line), and also against tunicamycin- or *N*-methyl-D-aspartate (NMDA)-induced retinal damage in mice was evaluated.

Methods. In vitro, BiP mRNA was measured after BIX treatment using semi-quantitative RT-PCR or real-time PCR. The effect of BIX on tunicamycin (at 2 μg/mL)-induced damage was evaluated by measuring the cell-death rate and CHOP protein expression. In vivo, BiP protein induction was examined by immunostaining. The retinal cell damage induced by tunicamycin (1 μg) or NMDA (40 nmol) was assessed by examining ganglion cell layer (GCL) cell loss, terminal deoxyribonucleotidyl transferase (TdT)-mediated dUTP nick-end labeling (TUNEL) staining, and CHOP protein expression.

Results. In vitro, BIX preferentially induced BiP mRNA expression both time- and concentration-dependently in RGC-5 cells. BIX (1 and 5 μM) significantly reduced tunicamycin-induced cell death, and BIX (5 μM) significantly reduced tunicamycin-induced CHOP protein expression. In vivo, intravitreal injection of BIX (5 nmol) significantly induced BiP protein expression in the mouse retina. Co-administration of BIX (5 nmol) significantly reduced both the retinal cell death and the CHOP protein expression in GCL induced by intravitreal injection of tunicamycin or NMDA.

Conclusions. These findings suggest that this BiP inducer may have the potential to be a therapeutic agent for endoplasmic reticulum (ER) stress-induced retinal diseases. (*Invest Ophthalmol Vis Sci.* 2009;50:334–344) DOI:10.1167/iovs.08-2123

The endoplasmic reticulum (ER) is the cellular organelle in which proteins (destined for secretion or for diverse subcellular localizations) are not only synthesized, but acquire their correct conformation. Perturbations of the environment normally required for protein folding in the ER, or the production of large amounts of misfolded proteins exceeding the functional capacity of the organelle, trigger a pattern of physiological response in the cell, collectively known as the unfolded protein response (UPR).[1–3] The UPR serves to cope with ER stress by transcriptionally regulating ER chaperones and other ER-resident proteins, attenuating the overall translation rate, and increasing the degradation of misfolded ER proteins. ER stress is caused by the accumulation of unfolded proteins in the ER lumen, and it is associated with various neurodegenerative diseases such as Alzheimer's, Huntington's, and Parkinson's diseases, and with type-1 diabetes.[1–6] Recent reports have shown that ER stress is also involved in a variety of experimental retinal neurodegenerative models, such as those of diabetic retinopathy,[7] retinitis pigmentosa,[8,9] and glaucoma.[10,11]

Recently, we reported that BiP expression is upregulated in the retina after intravitreal injection of either tunicamycin or NMDA (a glutamate-receptor agonist).[12,13] Tunicamycin, a glucosamine-containing nucleoside antibiotic, produced by genus *Streptomyces*, is an inhibitor of *N*-linked glycosylation and the formation of *N*-glycosidic protein-carbohydrate linkages.[14] Tunicamycin, which reduces the *N*-glycosylation of proteins, causes an accumulation of unfolded proteins in the ER and thus induces ER stress. Awai et al.[15] previously had demonstrated that NMDA induces CHOP protein (a member of the CCAAT/enhancer-binding protein family induced by ER stress) in GCL and the inner plexiform layer (IPL), and that CHOP$^{-/-}$ mice are more resistant to NMDA-induced retinal cell death than wild-type mice. These findings indicate that ER stress may be involved in these models of retinal injury.

BiP, a highly conserved member of the 70 kDa heat shock protein family, is one of the chaperones localized to the ER membrane,[16,17] and it is a major ER-luminal Ca^{2+}-storage protein.[18,19] BiP works to restore folding in misfolded or incompletely assembled proteins,[20–22] the interaction between BiP and misfolded proteins being dependent on its hydrophobic motifs.[23–25] Proteins stably bound to BiP are subsequently translocated from the ER into the cytosol, where they are degraded by proteasomes.[26,27] Previous reports have show that induction of BiP prevents the neuronal death induced by ER stress.[28–31] Hence, a selective inducer of BiP might attenuate ER stress and be a new, useful therapeutic agent for the treatment of ER stress-associated diseases.

This seemed an interesting idea, and we recently identified BiP inducer X (BIX) while screening for low molecular

From the Departments of [1]Biofunctional Evaluation, Molecular Pharmacology and [2]Medicinal Chemistry, Gifu Pharmaceutical University, Gifu, Japan; [3]Department of Psychiatry, Osaka University Graduate School of Medicine, Osaka, Japan; [4]Division of Molecular and Cellular Biology, Department of Anatomy, Faculty of Medicine, University of Miyazaki, Miyazaki, Japan; and [5]Department of Ophthalmology, University of Tokyo School of Medicine, Tokyo, Japan.

Supported in part by a Grant-in-Aid (No.18209053) for scientific research from the Ministry of Education, Science, Sports, Culture of the Japanese Government; by a research grant (No.18210101) from the Ministry of Health, Labor, and Welfare of the Japanese Government, and by Grant-in-Aid for Japan Society for the Promotion of Science Fellows.

Submitted for publication April 4, 2008; revised July 25, 2008; accepted October 27, 2008.

Disclosure: **Y. Inokuchi**, None; **Y. Nakajima**, None; **M. Shimazawa**, None; **T. Kurita**, None; **M. Kubo**, None; **A. Saito**, None; **H. Sajiki**, None; **T. Kudo**, None; **M. Aihara**, None; **K. Imaizumi**, None; **M. Araie**, None; **H. Hara**, None

The publication costs of this article were defrayed in part by page charge payment. This article must therefore be marked "*advertisement*" in accordance with 18 U.S.C. §1734 solely to indicate this fact.

Corresponding author: Hideaki Hara, Department of Biofunctional Evaluation, Molecular Pharmacology, Gifu Pharmaceutical University, 5-6-1 Mitahora-higashi, Gifu 502-8585, Japan; hidehara@gifu-pu.ac.jp.

Investigative Ophthalmology & Visual Science, January 2009, Vol. 50, No. 1

mass compounds that might induce BiP using high-throughput screening (HTS) with a BiP reporter assay system (Dual-Luciferase Reporter Assay; Promega Corporation, Madison, WI).[32] We found that BIX preferentially induced BiP mRNA and protein in SK-N-SH cells and reduced tunicamycin-induced cell death. Intracerebroventricular pretreatment with BIX reduced the infarction size after focal cerebral ischemia in mice. In view of the retinal research described above, we wondered whether BIX might reduce the retinal ganglion cell loss and CHOP expression induced by tunicamycin or NMDA treatment.

In the present study, we examined primarily whether induction of BiP might inhibit the retinal cell death induced by tunicamycin in RGC-5 cells in vitro, and/or that induced by tunicamycin or NMDA in mice in vivo.

Materials and Methods

All experiments were performed in accordance with the ARVO Statement for the Use of Animals in Ophthalmic and Vision Research, and they were approved and monitored by the Institutional Animal Care and Use Committee of Gifu Pharmaceutical University, Gifu, Japan.

Materials

Dulbecco modified Eagle medium (DMEM) and NMDA were purchased from Sigma-Aldrich (St. Louis, MO). The other drugs used and their sources were as follows: BIX, 1-(3,4-dihydroxyphenyl)-2-thiocyanatoethanone, was synthesized in the Department of Medicinal Chemistry, Gifu Pharmaceutical University, while tunicamycin was purchased from Wako (Osaka, Japan). Isoflurane was acquired from Nissan Kagaku (Tokyo, Japan) and fetal bovine serum (FBS) was from Valeant (Costa Mesa, CA).

RGC-5 Culture

RGC-5[32] were gifted by Neeraj Agarwal (Department of Pathology and Anatomy, UNT Health Science Center, Fort Worth, TX). Cultures of RGC-5 were maintained in DMEM supplemented with 10% FBS, 100 U/mL penicillin (Meiji Seika Kaisha Ltd., Tokyo, Japan), and 100 μg/mL streptomycin (Meiji Seika Kaisha. Ltd.) in a humidified atmosphere of 95% air and 5% CO_2 at 37°C. The RGC-5 cells were passaged by trypsinization every 3 days, as in our previous reports.[12,13,33] We used RGC-5 without any differentiation.

RNA Isolation and Semi-Quantitative RT-PCR Analysis

To examine the effect of BIX on BiP mRNA expression, RGC-5 cells were seeded in six-well plates at a density of 1.4×10^5 cells per well. After the cells had been incubating for 24 h, they were exposed to 50 μM BIX in 1% FBS DMEM for 0.5, 1, 2, 4, 6, 8, or 12 h, or to 2, 10, 50, or 150 μM BIX in 1% FBS DMEM for 6 h. Total RNA was extracted (RNeasy Mini Kit; QIAGEN KK, Tokyo, Japan) according to the manufacture's protocol. The total RNA was divided into microtubes, and frozen to −80°C. RNA concentrations were determined spectrophotometrically at 260 nm. First-strand cDNA was synthesized in a 20-μl reaction volume using a random primer (Takara, Shiga, Japan) and Moloney murine leukemia virus reverse transcriptase (Invitrogen, Carlsbad, CA). PCR was performed in a total volume of 30 μL containing 0.8 μM of each primer, 0.2 mM dNTPs, 3 U *Taq* DNA polymerase (Promega), 2.5 mM $MgCl_2$, and 1× PCR buffer. The amplification conditions for the semi-quantitative RT-PCR analysis were as follows: an initial denaturation step (95°C for 5 minutes), 20 cycles of 95°C for 1 minute, 55°C for 1 minute, and 72°C for 1 minute, and a final extension step (72°C for 7 minutes). The numbers of amplification cycles for the detection of BiP and β-actin were 18 and 15, respectively. The primers used for amplification were as follows: BiP: 5′-GTTTGCTGAGGAAGACAAAAAGCTC-3′ and 5′-CACTTCCATAGAGTTTGCTGATAATTG-3′; β-actin: 5′-TCCTCCCTGGAGAAGAGCTAC-3′ and 5′-TCCTGCTTGCTGATCCACAT-3′.

PCR products were resolved by electrophoresis through 6% (w/v) polyacrylamide gels. The density of each band was quantified using an imaging program (Scion Image Program; Scion Corporation, Frederick, MD).

Real-Time PCR

Real-time PCR (TaqMan; Applied Biosystems, Foster City, CA) was performed as described previously.[34] Single-stranded cDNA was synthesized from total RNA using a high-capacity cDNA archive kit (Applied Biosystems). Quantitative real-time PCR was performed using a sequence detection system (ABI PRISM 7900HT; Applied Biosystems) with a PCR master mix (TaqMan Universal PCR Master Mix; Applied Biosystems), according to the manufacturer's protocol. mRNA expression was measured by real-time PCR using a gene expression product (Assays-on-Demand Gene Expression Product; Applied Biosystems) and a BiP probe (Assay ID Details: Mm00517691). The thermal cycler conditions were as follows: 2 minutes at 50°C and then 10 minutes at 95°C, followed by two-step PCR for 50 cycles consisting of 95°C for 15 seconds followed by 60°C for 1 minute. For each PCR, we obtained the slope value, R^2 value, and linear range of a standard curve of serial dilutions. All reactions were performed in duplicate. The results are expressed relative to the β-actin (Assay ID Details: Mm00661904) internal control.

Cell Viability

To examine the effects of BIX on the cell death induced by tunicamycin (2 μg/mL) or staurosporine (an ER stress-independent apoptosis inducer, 30 nm) RGC-5 cells were seeded at a low density of 700 cells per well into 96-well plates. After pretreatment with BIX for 12 h, tunicamycin or staurosporine was added to the cultures for 48 h or 24 h, respectively. Cell death was assessed on the basis of combination staining with the fluorescent dyes Hoechst 33342 and propidium iodide (PI; Molecular Probes, Eugene, OR) or the change in fluorescence intensity after the cellular reduction of WST-8 to formazan. Hoechst 33342 (λex 350 nm, λem 461 nm) and PI (λex 535 nm, λem 617 nm) were added to the culture medium at final concentrations of 8 and 1.5 μM, respectively, for 30 minutes. Images were collected using a CCD camera (DP30VW; Olympus America, Center Valley, PA) via an epifluorescence microscope (IX70; Olympus, Tokyo, Japan) fitted with fluorescence filters for Hoechst 33342 (U-MWU; Olympus), and PI (U-MWIG; Olympus). In WST-8 assay, cell viability was assessed by culturing cells in a culture medium containing 10% WST-8 (Cell Counting Kit-8; Dojin Kagaku, Kumamoto, Japan) for 3 h at 37°C, with quantification being achieved by scanning with a microplate reader at 492 nm.[35] This absorbance is expressed as a percentage of that in control cells (which were in 1% FBS DMEM) after subtraction of background absorbance.

Animals

Mice used were male adult ddY mice (Japan SLC, Hamamatsu, Japan), male adult Thy-1-cyan fluorescent protein (CFP) transgenic mice (The Jackson Laboratory, Bar Harbor, Maine),[36] and ER stress-activated indicator (ERAI)-transgenic mice carrying the F-XBP1ΔDBD-venus, a variant of green fluorescent protein (GFP) fusion gene, which allows effective identification of cells under ER stress in vivo, as previously described by Iwawaki et al.[37] Briefly, when ER stress in ERAI transgenic mice was induced, splicing of mRNA encoding the XBP-1 fusion gene occurs and the spliced form of F-XBP1ΔDBD-venus fusion gene could be translated into fluorescent protein. Thus, it is visualized by the fluorescence intensity arising from the XBP-Δ-venus fusion protein during ER stress, and we measured it by fluorescence microscopy and immunoblotting in the present study.

All mice were kept under controlled lighting conditions (12 h:12 h light/dark). The mouse genotype was determined by applying standard PCR methodology to tail DNA.

NMDA- or Tunicamycin-Induced Retinal Damage

NMDA- or tunicamycin-induced retinal damage was produced as previously reported by Siliprandi et al. (1992).[38] Briefly, mice were anesthetized with 3.0% isoflurane and maintained with 1.5% isoflurane in 70% N_2O and 30% O_2 via an animal general anesthesia machine (Soft Lander; Sin-ei Industry Co. Ltd., Saitama, Japan). The body temperature was maintained between 37.0 and 37.5°C with the aid of a heating pad. Retinal damage was induced by the injection (2 μL/eye) of NMDA (Sigma-Aldrich) at 20 mM or tunicamycin at 1 μg/mL dissolved in 0.01 M PBS with 5% dimethyl sulfoxide (DMSO). Each solution was injected into the vitreous body of the left eye under the above anesthesia. One drop of 0.01% levofloxacin ophthalmic solution (Santen Pharmaceuticals Co. Ltd., Osaka, Japan) was applied topically to the treated eye immediately after the intravitreal injection. Seven days after the injection, eyeballs were enucleated for histologic analysis. For comparative purposes, nontreated retinas from each mouse strain were also investigated. BIX (0.5 or 5 nmol) or vehicle (5% DMSO in PBS) was co-administered with the NMDA or tunicamycin in each mouse.

Histologic Analysis

In mice under anesthesia produced by an intraperitoneal injection of sodium pentobarbital (80 mg/kg), each eye was enucleated and kept immersed for at least 24 h at 4°C in a fixative solution containing 4% paraformaldehyde. Six paraffin-embedded sections (thickness, 4 μm) cut through the optic disc of each eye were prepared in a standard manner and stained with hematoxylin and eosin. The damage induced by NMDA or tunicamycin was then evaluated, with three sections from each eye being used for the morphometric analysis, as described below. Light-microscope images were photographed, and the cells in the GCL at a distance between 375 and 625 μm from the optic disc were counted on the photographs in a masked fashion by a single observer (Y.I.). Data from three sections (selected randomly from the six sections) were averaged for each eye and used to evaluate the cell count in the GCL.

Retinal Flatmounts and Analysis in Transgenic Mice

Transgenic mice were given an overdose of sodium pentobarbital, and retinas were dissected out and fixed for 30 minutes in 4% paraformaldehyde diluted in 0.1 M phosphate buffer (PB) at pH 7.4. Retinas were subsequently washed with PBS at room temperature, flatmounted on clean glass slides using fluorescent mounting medium (Dako Corp., Carpinteria, CA), and stored in the dark at 4°C for 1 week. The damage induced by tunicamycin was then evaluated, with four sections (dorsal, ventral, temporal, and nasal) from each eye being used for the morphometric analysis, as described below. At various times after intravitreal injections (24 h in ERAI mice and 7 days in Thy-1-CFP transgenic mice), fluorescent images were photographed (×200, 0.144 mm^2) using an epifluorescence microscope (BX50; Olympus) fitted with a CCD camera (DP30VW; Olympus). In the case of Thy-1-CFP transgenic mice, Thy-1-CFP-positive cells at a distance of 1 mm from the optic disc were counted on the photographs in a masked fashion by a single observer (Y.I.). Data from the four parts of each eye were used to evaluate the RGC count.[39]

Immunostaining

Eyes were enucleated as described under Histologic Analysis, fixed in 4% paraformaldehyde overnight at 4°C, immersed in 25% sucrose for 48 h at 4°C, and embedded in optimum cutting temperature (OCT) compound (Sakura Finetechnical Co. Ltd, Tokyo, Japan). Transverse 10-μm thick cryostat sections were cut and placed onto slides (MAS COAT; Matsunami Glass Ind., Ltd., Osaka, Japan). Immunohistochemical staining was performed according to the following protocol: Briefly, tissue sections were washed in 0.01 M PBS for 10 minutes, and then endogenous peroxidase was quenched by treating the sections with 3% hydrogen peroxide in absolute methanol for 10 minutes, followed by a pre-incubation with 10% normal goat serum. They were then incubated overnight at 4°C with the following primary antibodies: against CHOP (1:1000 dilution in PBS; Santa Cruz, CA), and against BiP/GRP78 (1:1000 dilution in PBS; BD Transduction Laboratories, Lexington, KY). Sections were washed and then incubated with biotinylated anti-rabbit IgG or anti-mouse IgG. They were subsequently incubated with the avidin-biotin-peroxidase complex for 30 minutes, and then developed using diaminobenzidine (DAB) peroxidase substrate. Images were obtained using a digital camera (COOLPIX 4500; Nikon, Tokyo, Japan).

Quantitation of Density

In the DAB-labeled areas of anti-BiP/GRP78 (BD Transduction Laboratories) and anti-CHOP (Santa Cruz) in the GCL and IPL at a distance between 475 and 525 μm (50 × 50 μm) from the optic disc, retinal DAB-labeled cell density was evaluated by means of appropriately calibrated computerized image analysis, using median density in the range of 0 to 255 as an analysis tool (Image Processing and Analysis in Java, Image J; National Institute of Mental Health, Bethesda, MD) and averaged for two areas.[40] The data lie within the dynamic range of this assays

Briefly, light-microscope images of the above-mentioned areas were photographed, inverted in a gradation sequence using image editing software (Adobe Photoshop 5.5; Adobe Systems Inc., San Jose, CA), and then optical intensity was evaluated using Image J. The score for the negative-control (nontreated with first antibody), as the background value, was subtracted from the scores.

TUNEL Staining

TUNEL staining was performed according to the manufacturer's protocol (In Situ Cell Death Detection Kit; Roche Biochemicals, Mannheim, Germany) to detect the retinal cell death induced by NMDA. Mice were anesthetized with pentobarbital sodium at 80 mg/kg, IP, 24 h after intravitreal injection (either of NMDA 40 nmol/eye or of tunicamycin 1 μg/eye). The eyes were enucleated, fixed overnight in 4% paraformaldehyde, and immersed for 2 days in 25% sucrose with PBS. The eyes were then embedded in a supporting medium (OCT compound) for frozen-tissue specimens. Retinal sections at 10-μm thick were cut on a cryostat at −25°C, and stored at −80°C until staining. After twice washing with PBS, sections were incubated with terminal TdT enzyme at 37°C for 1 h, then washed 3 times in PBS for 1 minute at room temperature. Sections were subsequently incubated with an anti-fluorescein antibody-peroxidase conjugate at room temperature in a humidified chamber for 30 minutes, then developed using DAB tetrahydrochloride peroxidase substrate. Light-microscope images were photographed, and the labeled cells in the GCL at a distance between 375 and 625 μm from the optic disc were counted in two areas of the retina in a masked fashion by a single observer (Y.I.). The number of TUNEL-positive cells was averaged for these two areas, and plotted as the number of TUNEL-positive cells.

Western Blot Analysis

RGC-5 cells were lysed using a cell-lysis buffer (RIPA buffer R0278; Sigma-Aldrich) with protease (P8340; Sigma-Aldrich) and phosphatase inhibitor cocktails (P2850 and P5726; Sigma-Aldrich), and 1 mM EDTA. In vivo, mice were euthanatized using sodium pentobarbital at 80 mg/kg, IP, and their eyeballs were quickly removed. The retinas were carefully separated from the eyeballs and quickly frozen in dry ice. For protein extraction, the tissue was homogenized in the cell-lysis buffer using a homogenizer (Physcotron; Microtec Co. Ltd., Chiba, Japan). The lysate was centrifuged at 12,000*g* for 20 minutes, and the supernatant was used for this study. Assays to determine the protein concentration were performed by comparison with a known concentration of bovine serum albumin using a BCA protein assay kit (Pierce Biotechnology, Rockford, IL). A mixture of equal parts of an aliquot of

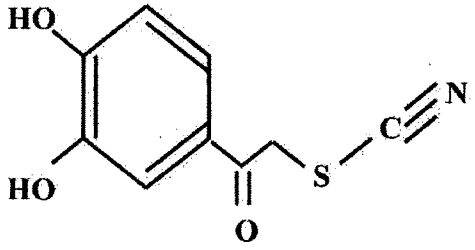

FIGURE 1. The structure of BIX (1-(3,4-dihydroxyphenyl)-2-thiocyanate-ethanone).

protein and sample buffer with 10% 2-mercaptoethanol was subjected to 10% sodium dodecyl sulfate-polyacrylamide gel electrophoresis. The separated protein was then transferred onto a polyvinylidene difluoride membrane (Immobilon-P; Millipore Corporation, Bedford, MA). For immunoblotting, the following primary antibodies were used: rabbit anti-CHOP polyclonal antibody (1:1000; Santa Cruz), mouse anti-β-actin monoclonal antibody (1:4000; Sigma-Aldrich), and rabbit anti-green fluorescent protein (GFP) polyclonal antibody (1:1000; Medical & Biological Laboratories Co. Ltd., Nagoya, Japan). The secondary antibody used was either goat anti-rabbit HRP-conjugated (1:2000) or goat anti-mouse HRP-conjugated (1:2000). The immunoreactive bands were visualized using a chemiluminescent substrate (SuperSignal West Femto Maximum Sensitivity Substrate; Pierce Biotechnology). The band intensity was measured using an imaging analyzer (Lumino Imaging Analyzer; Toyobo, Osaka, Japan) and a gel analysis electrophoresis analysis software (Gel Pro Analyzer; Media Cybernetics, Atlanta, GA).

Statistical Analysis

Data are presented as the means ± SE. Statistical comparisons were made by way of Dunnett's test or Student's *t*-test using statistical analysis software (STAT VIEW version 5.0; SAS Institute, Cary, NC). $P < 0.05$ was considered to indicate statistical significance.

RESULTS

BiP mRNA in RGC-5 Preferentially Induced by BIX

To clarify whether BIX (Fig. 1) induces BiP in RGC-5, we used semi-quantitative RT-PCR and real-time PCR, using a specific primer and a TaqMan probe recognizing BiP mRNA, respectively. Real-time PCR revealed that the level of BiP mRNA was significantly elevated at 0.5 to 12 h (peak at approximately 6 h) after treatment with 50 μM BIX (Fig. 2A). At 6 h after treatment with BIX (2 to 150 μM), BiP mRNA was increased concentration-dependently (Fig. 2B). Next, we used real-time *PCR* to investigate whether BIX might affect the expressions of any other genes related to the ER stress response, such as GRP94, calreticulin, protein kinase inhibitor of 58 kDa ($p58^{IPK}$), or asparagine synthetase (ASNS; Fig. 2C). Real-time PCR revealed significant inductions of ASNS and calreticulin mRNAs at 6 h after treatment with BIX at 2 and 10 μM, respectively. At 50 μM, BIX induced the mRNAs for GRP94 at 12 h, calreticulin at 6 and 12 h, $p58^{IPK}$ at 6 h, and ASNS at 12 h. In contrast, GRP94 mRNA was significantly reduced at 4 h after treatment with 50 μM BIX.

Protective Effect of BIX against ER Stress–Induced Cell Death in RGC-5 Cells

To investigate whether BIX can prevent the cell death induced by ER stress, RGC-5 cells were pretreated for 12 h with or without BIX, then treated with 2 μg/mL tunicamycin, and finally incubated for a further 48 h. Fluorescence micrographs of Hoechst 33342 and PI staining revealed 38.4 ± 4.5% cell death ($n = 8$) at 48 h after tunicamycin treatment, (control: 0.9 ± 0.2%, $n = 8$), and pretreatment with BIX at 1 and 5 μM significantly reduced this cell death (Figs. 3A, 3B). Next, we evaluated the expression of CHOP protein after tunicamycin treatment. There was no CHOP protein expression in either nontreated or BIX-treated cells (Figs. 3C, 3D). On the other

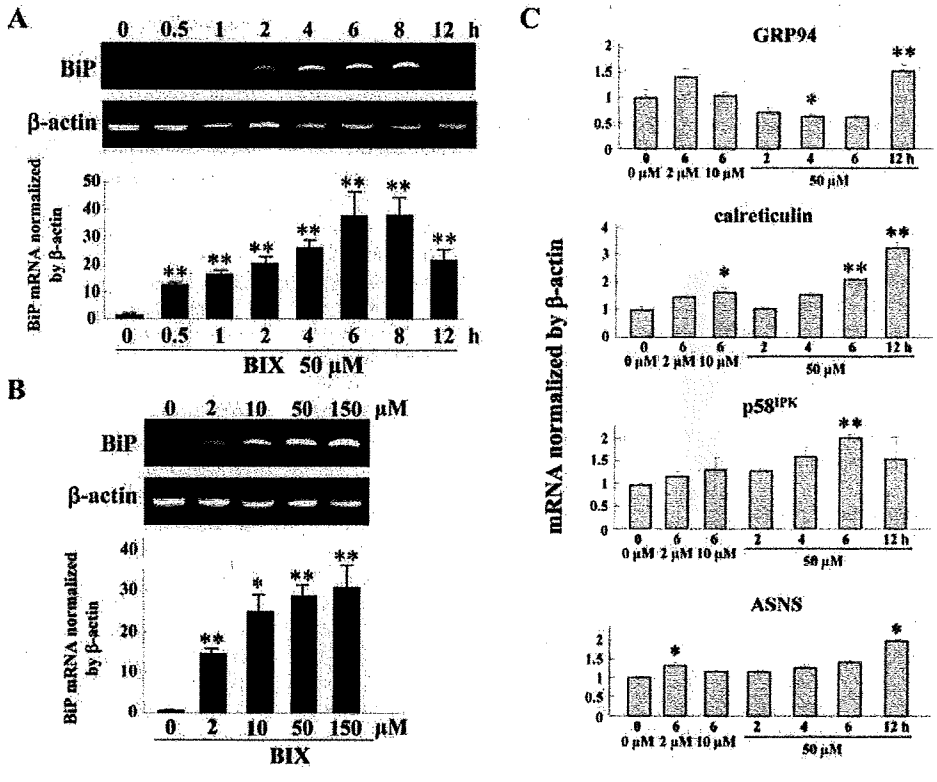

FIGURE 2. Effect of BIX on BiP mRNA expression BIX in RGC-5 cells. (A) Time-dependent induction of BiP mRNA after treatment with 50 μM BIX and (B) concentration-dependence of BIX-induced BiP mRNA expression are each shown by semi-quantitative RT-PCR (*upper panel*) and real-time PCR (*lower panel*). β-Actin mRNA is shown as an internal control. (C) Induction of GRP94, calreticulin, $p58^{IPK}$, and ASNS mRNAs at 6 h after treatment with 2 or 10 μM BIX and at 2 to 12 h after treatment with 50 μM BIX. Data are shown as mean ± SE ($n = 3$ or 4). $^*P < 0.05$, $^{**}P < 0.01$ versus 0 μM (A and B) or 0 μM/0 h (C).

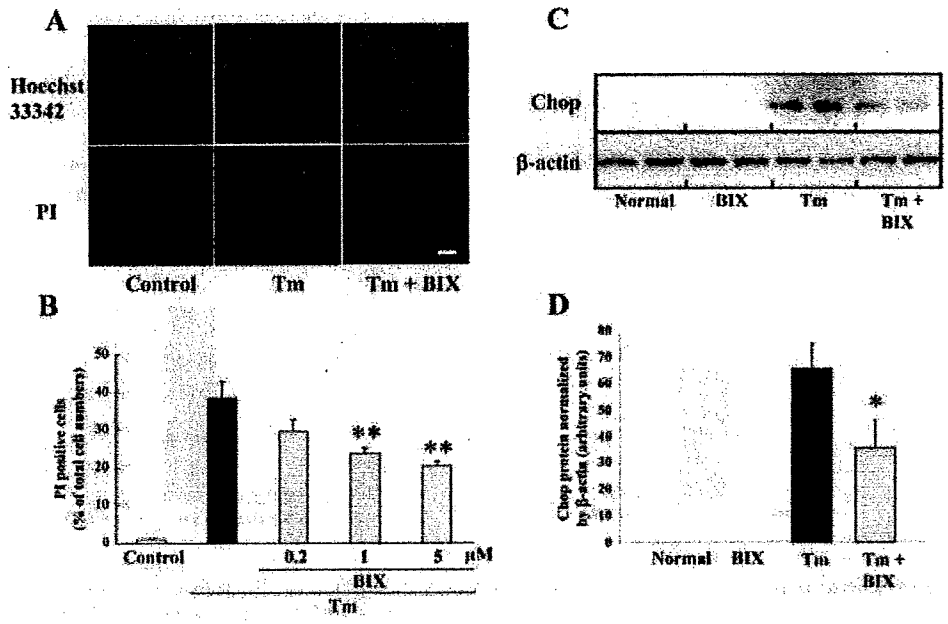

FIGURE 3. Effects of BIX on tunicamycin-induced cell death and CHOP protein expression in RGC-5 cells. (A) RGC-5 cells were pretreated with vehicle or with 1 μM BIX for 12 h, and then immersed in fresh medium (control) or in medium supplemented with 2 μg/mL tunicamycin (Tm; labeled Tm or Tm + BIX). *Upper* photomicrographs show Hoechst 33342 and *lower* ones propidium iodide (PI) staining at 48 h after tunicamycin stimulation. Scale bar represents 25 μm. (B) Numbers of PI-positive cells after tunicamycin treatment. Pretreatment of cells with BIX (1 and 5 μM) significantly reduced the amount of cell death (vs. cells treated with tunicamycin alone). (C) Immunoblot of CHOP protein shows that tunicamycin induced significant CHOP expression, and that pretreatment of cells with BIX at 5 μM reduced this expression with no change in the level of β-actin. *Upper panel* shows CHOP and *lower panel* shows β-actin. (D) Quantitative representations of β-actin-based tunicamycin-induced CHOP protein expression (in arbitrary units). Data are shown as mean ± SE (n = 6 or 8). $^*P < 0.05$, $^{**}P < 0.01$ versus tunicamycin alone.

hand, tunicamycin markedly induced CHOP protein, while pretreatment with BIX at 5 μM reduced this expression to almost half the value seen after tunicamycin treatment alone (Figs. 3C, 3D).

Effects of BIX on Cell Damage Induced by Staurosporine in RGC-5 Culture

To investigate whether BIX protects non-ER stress-induced cell death, we examined staurosporine-induced cell death. Staurosporine at 30 nM for 24 h reduced cell viability to approximately 60% of control (Fig. 4). There was no statistical difference between BIX (1 and 5 μM)-treated and vehicle-treated group.

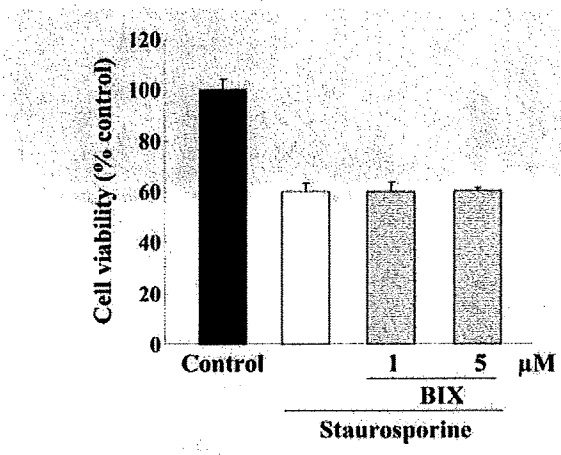

FIGURE 4. Effect of BIX on the cell death induced by staurosporine in RGC-5. RGC-5 cells were pretreated with vehicle or with BIX (1 or 5 μM) for 12 h, and then immersed in fresh medium (control) or in medium supplemented with staurosporine at 30 nM. At the end of this culture period, cell death was assessed by WST-8 assay (Cell Counting Kit-8; Dojin Kagaku). Data are shown as mean ± SE (n = 6).

BiP Protein in the Mouse Retina Induced by Intravitreous Injection of BIX

Compared with that in the nontreated retina, BiP protein expression in GCL and IPL was significantly increased at 6 and 12 h after intravitreal injection of BIX (5 nmol; Figs. 5A, 5B). Optical density analysis confirmed that administration of BIX induced BiP protein in vivo (Fig. 5D).

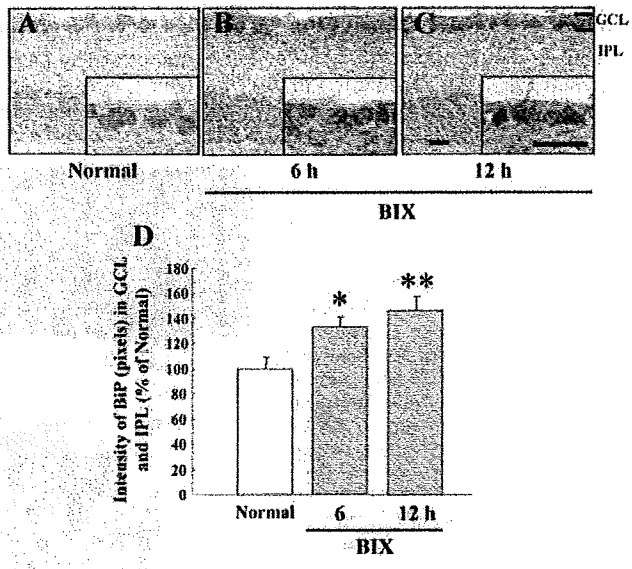

FIGURE 5. BiP protein expression in the mouse retina induced by intravitreous injection of BIX. Immunostaining probed with an antibody against BiP/GRP78. (A) Nontreated, (B) 6 h, and (C) 12 h after intravitreous injection of BIX (5 nmol). (D) Expression ratio for BiP induction intravitreous injection of BIX is represented as the ratio of intensity values. Data are shown as mean ± SE (n = 6). $^*P < 0.05$, $^{**}P < 0.01$ versus nontreated normal retina. Each scale bar represents 25 μm.

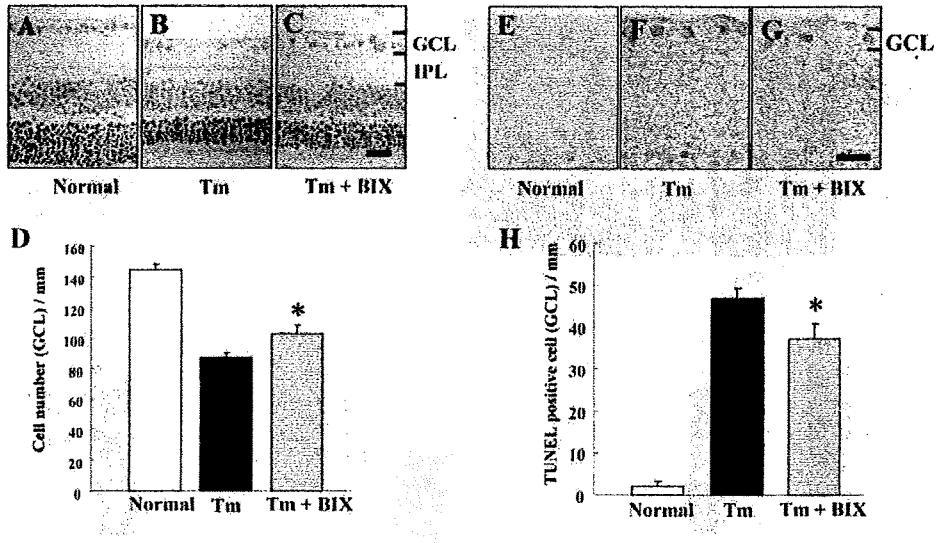

FIGURE 6. Effects of BIX on retinal damage induced by intravitreal injection of tunicamycin in mice. Hematoxylin and eosin staining of cross-sections of (A) nontreated, (B) Tm-treated, and (C) Tm plus BIX-treated mouse retinas at seven days after intravitreal injection of tunicamycin (1 μg) either alone or with BIX (5 nmol). (D) Damage was evaluated by counting cell numbers in GCL at seven days after the above injections. TUNEL staining of cross-sections of (E) nontreated, (F) Tm-treated, and (G) Tm plus BIX-treated mouse retinas at seven days after the above injections. (H) Effect of BIX on Tm-induced expression of TUNEL-positive cells at 24 h after the above injections. Data are shown as mean ± SE (n = 9 or 10). *$P < 0.05$ versus tunicamycin alone. Scale bars each represent 25 μm.

Protective Effect of BIX against Tunicamycin-Induced Retinal Damage in Mice

Tunicamycin decreased the cell number in GCL at 7 days after its intravitreal injection (vs. nontreated retinas; Figs. 6A, 6B). There was significantly less cell loss in GCL when BIX (5 nmol) was co-administered with the tunicamycin (Figs. 6B–6D). In addition, intravitreal injection of tunicamycin increased the number of TUNEL-positive cells in GCL at 24 h (vs. nontreated retinas; Figs. 6E, 6F). BIX (5 nmol), when co-administered with the tunicamycin, significantly reduced the number of TUNEL-positive cells (vs. tunicamycin alone; Figs. 6F–6H).

Protective Effect of BIX against Tunicamycin-Induced Retinal Damage in Thy-1-CFP Transgenic Mice

In this experiment on Thy-1-CFP transgenic mice, we confirmed the effect of BIX in a larger retinal area than that evaluated in Figure 6D. We counted the number of Thy-1-CFP-positive cells (in flatmounts) in the four white areas shown 1 mm from the center of the optic disc in Figure 7E, and then totaled these values. In the Thy-1-CFP–transgenic mouse retina, axonal fibers were evenly and densely distributed. There were congested CFP-positive cells in the vehicle-treated retina (Fig. 7A), and no change was observed in BIX-treated retinas without tunicamycin treatment (Fig. 7B). Intravitreal injection of tunicamycin decreased the Thy-1-CFP–positive cell count at 7 days (vs. vehicle-treated retina; Figs. 7A, 7C). BIX at 5 nmol, when co-administered with the tunicamycin, significantly inhibited this cell loss (Figs. 7C, 7D, 7F).

Effect of BIX on Tunicamycin-Induced CHOP Expression in Mice

Representative photograph of a nontreated retina is shown in Figure 8A. No change was observed in the BIX-treated retina (Fig. 8B). Optical density analysis of CHOP protein immunoreactivity in GCL and IPL showed that intravitreal injection of tunicamycin (1 μg) significantly increased the level of CHOP protein at 72 h after the injection (Fig. 8C). BIX (5 nmol), when co-administered with the tunicamycin, significantly inhibited this effect (Figs. 8D, 8E).

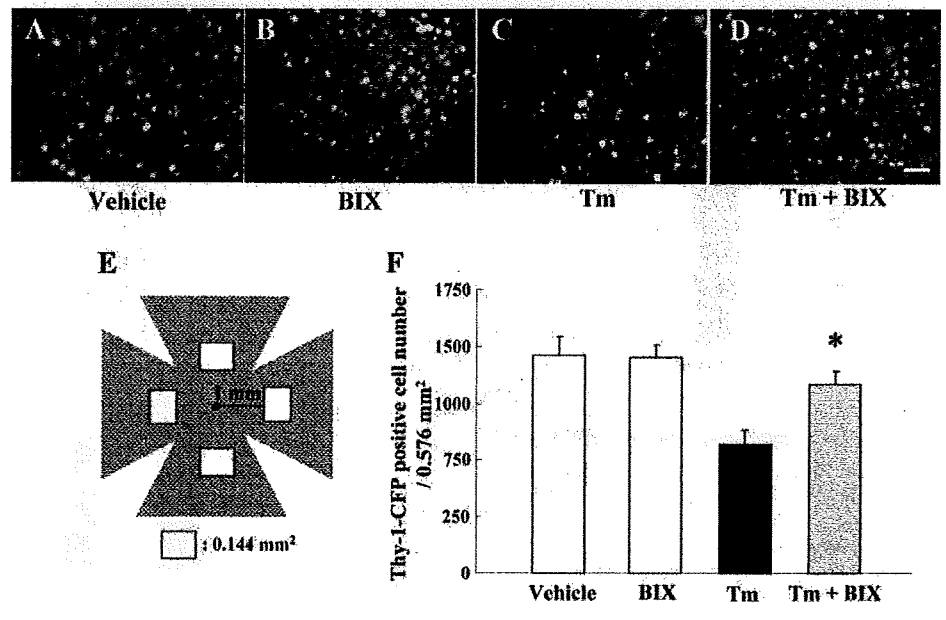

FIGURE 7. Effects of BIX on retinal damage induced by intravitreal injection of tunicamycin in Thy-1-CFP transgenic mice. Mouse retinas (flatmounts) at seven days after intravitreal injection of (A) vehicle, (B) BIX (5 nmol), (C) Tm (1 μg), or (D) Tm (1 μg) plus BIX (5 nmol). Damage was evaluated by counting Thy-1-CFP–positive cell numbers in the four *white* areas shown in (E) (each area 0.144 mm^2 × 4 areas; total 0.576 mm^2) at seven days after the above intravitreal injections. (F) Effect of BIX against Tm-induced damage (indicated by decreased number of Thy-1-CFP–positive cells) at seven days after intravitreal injection. Data are shown as mean ± SE (n = 9 or 10). *$P < 0.05$ versus tunicamycin alone. Scale bar represents 25 μm.

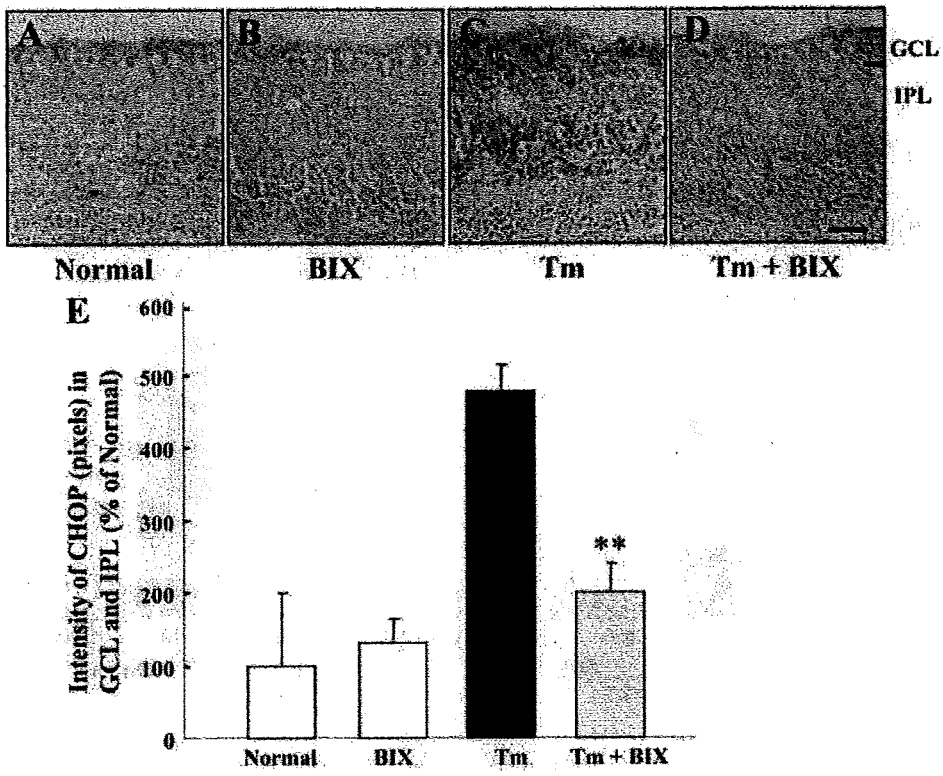

FIGURE 8. Effect of BIX on tunicamycin-induced CHOP expression in the mouse retina. Mouse retinas (cross-sections) either (A) nontreated or at three days after intravitreal injection of (B) BIX (5 nmol), (C) Tm (1 μg) or (D) Tm (1 μg) plus BIX (5 nmol). (E) Relative density of CHOP protein expression in GCL and IPL at three days after the above intravitreal injections. Data are shown as mean ± SE ($n = 6$). $^{**}P < 0.01$ versus tunicamycin alone. Scale bar represents 25 μm.

Effect of BIX on Tunicamycin-Induced XBP-1 Expression in ERAI Mice

In ERAI mice, the fluorescence intensity arising from the XBP-1-venus fusion protein (indicating ER stress activation) can be easily visualized, allowing evaluation of the effect of ER stress on the retina. In the representative photographs of flatmount retinas from ERAI mice shown in Figure 9, no difference was observed between vehicle-treated and BIX-treated retinas (Fig. 9B). Intravitreal injection of tunicamycin (1 μg) induced XBP-1-venus expression (vs. the vehicle-treated retina; Fig. 9C). Immunoblot analysis of XBP-1-venus protein expression in the retina (using an anti-GFP antibody) showed that intravitreal injection of tunicamycin (1 μg) significantly raised the level of XBP-1-venus protein, and that BIX (5 nmol), when co-administered with the tunicamycin (Fig. 9D), significantly inhibited this effect (Figs. 9E, 9F).

Protective Effect of BIX against NMDA-Induced Retinal Damage in Mice

A representative photograph of a nontreated retina is shown in Figure 10A. Intravitreal injection of NMDA (a) decreased the

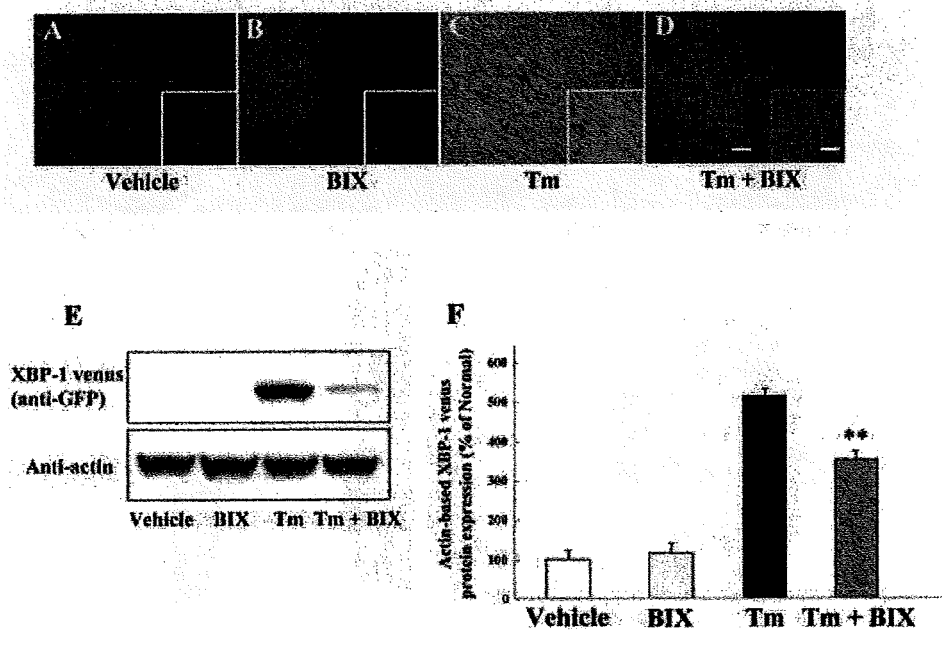

FIGURE 9. Effect of BIX on tunicamycin-induced XBP-1 venus expression in ERAI mice. Mouse retinas (flatmounts) at 24 h after intravitreal injection of (A) vehicle, (B) BIX (5 nmol), (C) Tm (1 μg) or (D) Tm (1 μg) plus BIX (5 nmol). (E) *Upper panel* shows XBP-1 venus protein expression, while *lower panel* shows β-actin protein expression at 24 h after the above injections. (F) Western blot analysis showing effect of BIX on Tm-induced expression of β-actin-based XBP-1 venus protein expression at 24 h after the above injections. Data are shown as mean ± SE ($n = 8$). $^{*}P < 0.01$ versus tunicamycin alone. Scale bars in main photomicrographs and in *insets* represent 25 and 5 μm, respectively.

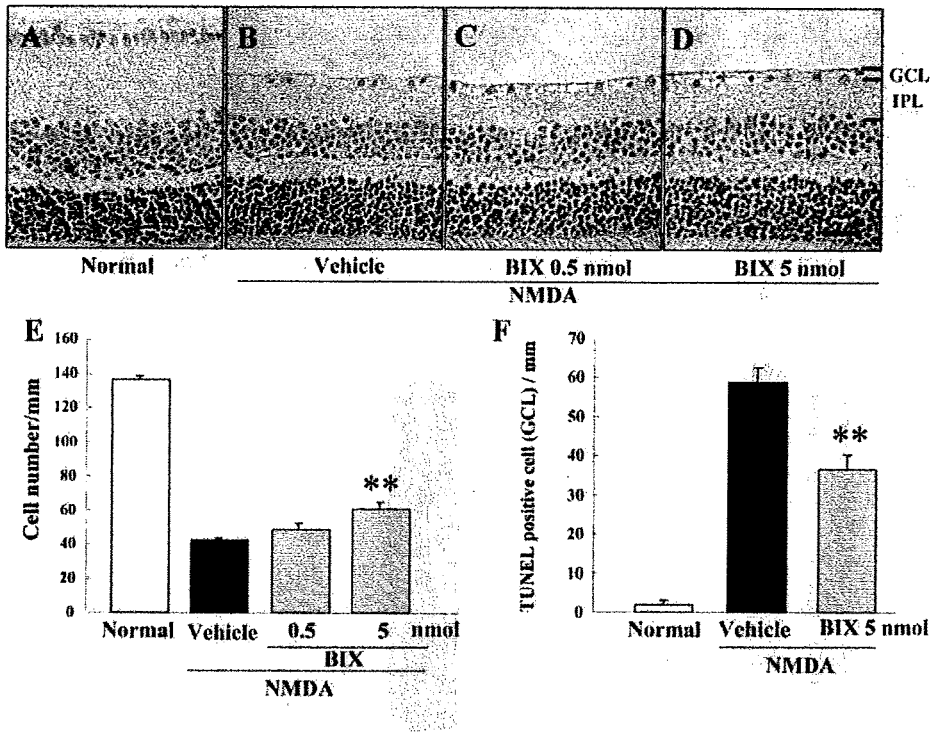

FIGURE 10. Effects of BIX on retinal damage induced by intravitreal injection of NMDA in mice. Mouse retinas (cross-sections) either (A) nontreated or at seven days after intravitreal injection of (B) NMDA (40 nmol) alone or (C, D) NMDA (40 nmol) plus BIX (0.5 or 5 nmol). (E) Damage was evaluated by counting cell numbers in GCL at seven days after the above intravitreal injections. (F) Effect of BIX on NMDA-induced expression of TUNEL-positive cells at 24 h after intravitreal injection of NMDA (40 nmol) either alone or with BIX (5 nmol). Data are shown as mean ± SE (n = 9 or 10). $^{**}P < 0.01$ versus NMDA-treated control group. Scale bar represents 25 μm.

cell number in GCL at 7 days (Figs. 10B, 10E) and (b) increased the number of TUNEL-positive cells in GCL at 24 h (vs. nontreated normal retina; Fig. 10F). BIX (5 nmol), when co-administered with the NMDA, significantly reduced (vs. NMDA alone) both the cell loss in GCL (Figs. 10D, 10E) and the number of TUNEL-positive cells (Fig. 10F). On the other hand, there was no statistical difference between BIX (0.5 nmol)- and vehicle-treated group in NMDA-induced cell death in GCL (Figs. 10C, 10E).

Effect of BIX on NMDA-Induced CHOP Expression in Mice

A representative photograph of a nontreated retina is shown in Figure 11A and no change was detected between nontreated

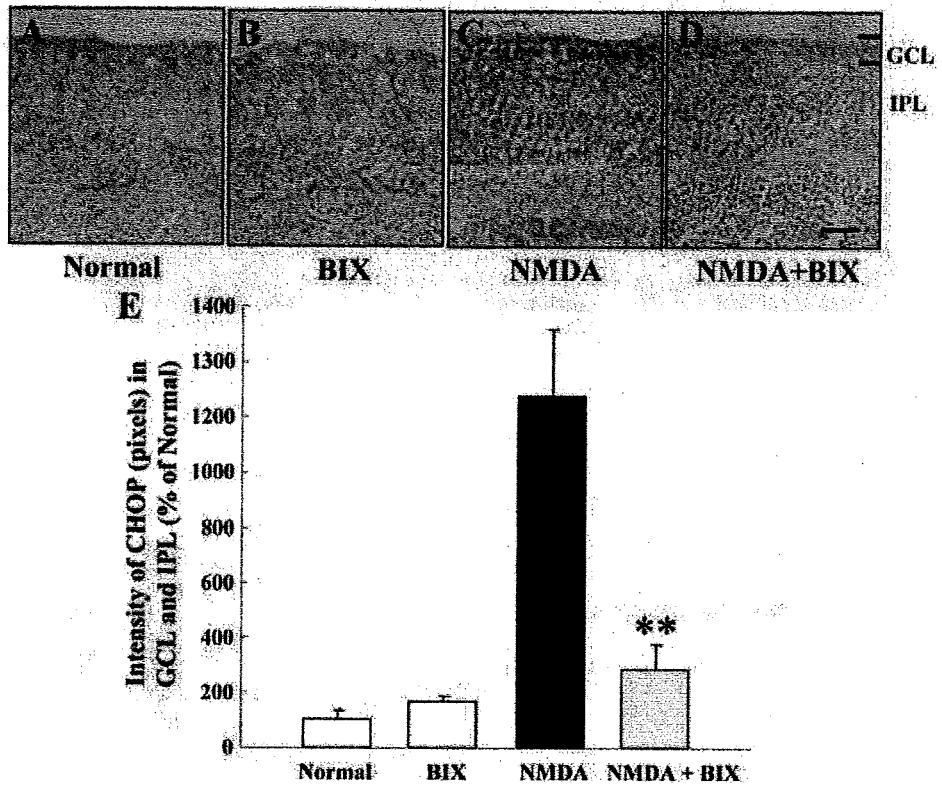

FIGURE 11. Effect of BIX on NMDA-induced CHOP expression in mice. Mouse retinas (cross-sections) either (A) nontreated or at three days after intravitreal injection of (B) NMDA (40 nmol) alone or (C) NMDA (40 nmol), or (D) NMDA (40 nmol) plus BIX (5 nmol). (E) Relative density of CHOP protein expression in GCL and IPL at three days after the above intravitreal injections. Data are shown as mean ± SE (n = 6). $^{**}P < 0.01$ versus NMDA alone. Scale bar represents 25 μm.

retina and the BIX-treated retina without NMDA treatment (Figs. 11A, 11B). Optical density analysis of CHOP protein immunoreactivity in GCL and IPL showed that intravitreal injection of NMDA (40 nmol) significantly increased the level of CHOP protein at 72 h after the injection (Fig. 11C). When co-administered with the NMDA, BIX (5 nmol) significantly inhibited this effect (Figs. 11D, 11E).

Discussion

In the present study, we confirmed that BIX preferentially induces BiP mRNA in RGC-5. Although it also induced GRP94, calreticulin, p58^{IPK}, and ASNS, these inductions were lower than that of BiP. This is consistent with our previous study that BIX preferentially induced BiP with slight inductions of GRP94, calreticulin, and CHOP mediated by the activating transcription factor 6 (ATF6) pathway accompanied by activation of ERSEs, and that BIX does not affect the pathway downstream of IRE1 or the translational control branch downstream of PERK in SK-N-SH cells.[32] Therefore, BIX is not just an ER stressor such as tunicamycin or thapsigargin, and we consider that the induction of BiP by BIX is mediated by the ATF6 pathway in RGC-5 similar to that in SK-N-SH cells. Next, we evaluated the effects of BIX, as a preferential inducer of BiP, on ER stress-induced in vitro cell death in RGC-5 (a rat ganglion cell-line) and in vivo retinal damage in mice. We found that BIX reduced tunicamycin-induced cell death in RGC-5 and also reduced both tunicamycin-induced and NMDA-induced retinal damage in mice. Our previous study revealed that BIX (a) reduced tunicamycin-induced cell death in SK-N-SH cells, (b) contributed to the induction of BiP expression via the ATF-6 pathway (but not via the PERK or IRE1 pathways), and (c) on intracerebroventricular injection, prevented the neuronal damage induced by focal ischemia in mice.[32] Furthermore, immunostaining revealed that intravitreal injection of BIX significantly induced BiP protein in mouse retina. Particularly, it expressed in GCL and IPL (versus both the normal and the sham retina). On the other hand, there was little protective effect of BIX against RGC-5 damages after staurosporine treatment. Staurosporine is well known as a nonspecific inhibitor of protein kinases and initiates caspase-dependent apoptosis in many cell types.[41,42] Our previous studies revealed that staurosporine induced cell death without any changes in the expression of BiP or CHOP protein.[12,43] Furthermore, preliminary study showed that treatment with BIX (1 and 5 μM) did not inhibit RGC-5 cell death 48 h after serum deprivation, which does not induce any UPR-responses such as BiP or CHOP (unpublished data). These results strongly support that BIX selectively protects cell damage induced by ER stress.

Recently, we reported that in mice, increased expressions of XBP-1 splicing, BiP, and CHOP could be detected after the induction of retinal damage by tunicamycin, NMDA, or an elevation of intraocular pressure.[13] That report was the first to demonstrate an involvement of ER stress and BiP in retinal cell death in mice. Hence, in the present study we asked whether BIX can prevent such retinal damage. By histologic analysis and TUNEL staining, we estimated that BIX reduced tunicamycin-induced retinal damage in GCL. However, the cell counts in partial cross sections provide a comparatively small sample on which quantitative morphometry can be used to judge such an effect. Therefore, we used Thy-1-CFP transgenic mice[36] to examine the effect of BIX in a large retinal area. This transgene contains a CFP gene under the direction of regulatory elements derived from the mouse Thy-1 gene, and the transgenic mice express CFP protein in RGC and in the inner part of the IPL of the retina.[36] Our results show that BIX exerted a protective effect against tunicamycin-induced retinal damage in the Thy-1-CFP transgenic mouse. However, it is possible that microglial cells become co-labeled with CFP by phagocytosis of the dying RGCs. In this study, we evaluated CFP-positive cells in 7 days after tunicamycin injection. In our previous and preliminary studies, activated microglia cells in GCL were increased at 3 days after NMDA injection[13] and their increases were almost ceased within the 7 days (unpublished data). Furthermore, microglial cells can be distinguished with neuronal cells by their morphologic features.[44] In fact, microglial cells were scarcely observed at seven days after tunicamycin injection, similar to that at seven days after NMDA injection. When we investigated the effect of BIX on NMDA-induced retinal damage in ddY mice, we found that it significantly attenuated such damage. NMDA is well known to induce RGC death and optic-nerve loss (effects mediated by excitatory glutamate receptor), and such neuronal death is believed to play a role in many neurologic and neurodegenerative diseases.[45,46] Recently, Uehara et al.[47] noted that mild exposure to NMDA induced apoptotic cell death in primary cortical culture, and they demonstrated this effect to be caused by an accumulation of polyubiquitinated proteins and increases in XBP-1 mRNA splicing and CHOP mRNA (reflecting activation of the UPR signaling pathway). They also found that protein-disulphide isomerase, which assists in the maturation and transport of unfolded secretory proteins, prevented the neurotoxicity associated with ER stress. These findings suggested that activation of ER stress may participate in the retinal cell death occurring after NMDA-receptor activation and/or an ischemic insult.[47]

In our investigation of the mechanisms underlying the above-mentioned effects, we focused on CHOP. Since CHOP is a member of the CCAAT/enhancer-binding protein family that is induced by ER stress and participates in ER-mediated apoptosis, CHOP may be a key molecule in retinal cell death.[48] We found that treatment with tunicamycin induced apoptotic cell death in RGC-5 and also induced a production of ER stress-related proteins (BiP, the phosphorylated form of eIF2α, and CHOP protein). BIX reduced both the cell death and the CHOP protein expression induced by tunicamycin in RGC-5 in vitro. BIX also attenuated the CHOP protein expression induced by either tunicamycin or NMDA in the mouse retina in vivo. As mentioned above, BIX may affect CHOP protein expression through ATF6 pathway, but no change was observed in BIX-treated RGC-5. In our previous data in SK-N-SH cells, BIX slightly increased CHOP mRNA only at 2 h after the treatment. Expression of CHOP is mainly regulated by three transcription factors—ATF4, cleaved ATF6, and x-box binding protein-1 (XBP-1)—which are downstream effectors during ER stress in similar to other ER chaperones. These differences between BiP and CHOP expression by BIX may be due to the difference of their promoters. CHOP promoter contains at least two ERSE motifs (CHOP ERSE-1 and CHOP ERSE-2) located in opposite directions with a 9 bp overlap, and one of ERSEs is inactive.[49] On the other hand, BiP promoter has three functional ERSE motifs of the rat GRP78 promoter (ERSE-163, ERSE-131, and ERSE-98).[50] These variations in each promoter may contribute to the differences among the expressions of ER chaperons induced by BIX and the lack of CHOP expression.

Subsequently, we monitored XBP-1 activation in the mouse retina in vivo, using ERAI transgenic mice.[37] Effective identification of cells under ER stress conditions is possible in the retina in these mice, as described in our previous report.[13] Here, ERAI mice carrying the F-XBP1ΔDBD-venus expression gene were used to monitor ER stress. The fluorescence intensity arising from the X-box binding protein (XBP1)-venus fusion protein, indicating ER stress activation, was increased in cells within GCL and IPL at 24 h after injection of tunicamycin into the vitreous. BIX significantly reduced this expression, indicating that BIX may attenuate the retinal damage induced

by ER stress-associated factors. In our previous study,[32] we found that BIX induced BiP protein expression via the ATF-6 pathway (not via other ER stress-associated factors such as the PERK and IRE1 pathways) in SK-N-SH cells. Possibly, the protective mechanism underlying the effect of BIX on the mouse retina may be the same as that revealed by our previous study, but further experiments will be needed to clarify this issue.

In conclusion, we have demonstrated that BIX, a preferential inducer of BiP, inhibits both the neuronal cell death induced by ER stress in vitro in RGC-5 cells and in vivo in the mouse retina. Hence, an increase in BiP might be one of the targets of mechanisms bestowing neuroprotection in retinal diseases.

Acknowledgments

The authors thank Masayuki Miura (Department of Genetics, Graduate School of Pharmaceutical Sciences, University of Tokyo, Tokyo, Japan) for the kind gift of ERAI mice, and Rumi Uchibayashi and Shunsake Imai for technical assistance.

References

1. Travers KJ, Patil CK, Wodicka L, Lockhart DJ, Weissman JS, Walter P. Functional and genomic analyses reveal an essential coordination between the unfolded protein response and ER-associated degradation. *Cell.* 2000;101:249–258.
2. Harding HP, Novoa I, Zhang Y, et al. Regulated translation initiation controls stress-induced gene expression in mammalian cells. *Mol Cell.* 2000;6:1099–1108.
3. Schroder M, Kaufman RJ. The mammalian unfolded protein response. *Annu Rev Biochem.* 2005;74:739–789.
4. Katayama T, Imaizumi K, Honda A, et al. Disturbed activation of endoplasmic reticulum stress transducers by familial Alzheimer's disease-linked presenilin-1 mutations. *J Biol Chem.* 2001;276:43446–43454.
5. Ryu EJ, Harding HP, Angelastro JM, Vitolo OV, Ron D, Greene LA. Endoplasmic reticulum stress and the unfolded protein response in cellular models of Parkinson's disease. *J Neurosci.* 2002;22:10690–10698.
6. Oyadomari S, Koizumi A, Takeda K, et al. Targeted disruption of the Chop gene delays endoplasmic reticulum stress-mediated diabetes. *J Clin Invest.* 2002;109:525–532.
7. Roybal CN, Yang S, Sun CW, et al. Homocysteine increases the expression of vascular endothelial growth factor by a mechanism involving endoplasmic reticulum stress and transcription factor ATF4. *J Biol Chem.* 2004;279:14844–14852.
8. Rebello G, Ramesar R, Vorster A, et al. Apoptosis-inducing signal sequence mutation in carbonic anhydrase IV identified in patients with the RP17 form of retinitis pigmentosa. *Proc Natl Acad Sci USA.* 2004;101:6617–6622.
9. Lin JH, Li H, Yasumura D, et al. IRE1 signaling affects cell fate during the unfolded protein response. *Science.* 2007;318:944–949.
10. Joe MK, Sohn S, Hur W, Moon Y, Choi YR, Kee C. Accumulation of mutant myocilins in ER leads to ER stress and potential cytotoxicity in human trabecular meshwork cells. *Biochem Biophys Res Commun.* 2003;312:592–600.
11. Gould DB, Marchant JK, Savinova OV, Smith RS, John SW. Col4a1 mutation causes endoplasmic reticulum stress and genetically modifiable ocular dysgenesis. *Hum Mol Genet.* 2007;16:798–807.
12. Shimazawa M, Ito Y, Inokuchi Y, Hara H. Involvement of double-stranded RNA-dependent protein kinase in ER stress-induced retinal neuron damage. *Invest Ophthalmol Vis Sci.* 2007;48:3729–3736.
13. Shimazawa M, Inokuchi Y, Ito Y, et al. Involvement of ER stress in retinal cell death. *Mol Vis.* 2007;13:578–587.
14. Mahoney WC, Duksin D. Biological activities of the two major components of tunicamycin. *J Biol Chem.* 1979;254:6572–6576.
15. Awai M, Koga T, Inomata Y, et al. NMDA-induced retinal injury is mediated by an endoplasmic reticulum stress-related protein, CHOP/GADD153. *J Neurochem.* 2006;96:43–52.
16. Lee YK, Brewer JW, Hellman R, Hendershot LM. BiP and immunoglobulin light chain cooperate to control the folding of heavy chain and ensure the fidelity of immunoglobulin assembly. *Mol Biol Cell.* 1999;10:2209–2219.
17. Li WW, Alexandre S, Cao X, Lee AS. Transactivation of the grp78 promoter by Ca^{2+} depletion. A comparative analysis with A23187 and the endoplasmic reticulum Ca^{2+}-ATPase inhibitor thapsigargin. *J Biol Chem.* 1993;268:12003–12009.
18. van de Put FH, Elliott AC. The endoplasmic reticulum can act as a functional Ca^{2+} store in all subcellular regions of the pancreatic acinar cell. *J Biol Chem.* 1997;272:27764–27770.
19. Lievremont JP, Rizzuto R, Hendershot L, Meldolesi J. BiP, a major chaperone protein of the endoplasmic reticulum lumen, plays a direct and important role in the storage of the rapidly exchanging pool of Ca^{2+}. *J Biol Chem.* 1997;272:30873–30879.
20. Helenius A. How N-linked oligosaccharides affect glycoprotein folding in the endoplasmic reticulum. *Mol Biol Cell.* 1994;5:253–265.
21. Kuznetsov G, Chen LB, Nigam SK. Multiple molecular chaperones complex with misfolded large oligomeric glycoproteins in the endoplasmic reticulum. *J Biol Chem.* 1997;272:3057–3063.
22. Klausner RD, Sitia R. Protein degradation in the endoplasmic reticulum. *Cell.* 1990;62:611–614.
23. Blond-Elguindi S, Cwirla SE, Dower WJ, et al. Affinity panning of a library of peptides displayed on bacteriophages reveals the binding specificity of BiP. *Cell.* 1993;75:717–728.
24. Knarr G, Gething MJ, Modrow S, Buchner J. BiP binding sequences in antibodies. *J Biol Chem.* 1995;270:27589–27594.
25. Knarr G, Modrow S, Todd A, Gething MJ, Buchner J. BiP-binding sequences in HIV gp160. Implications for the binding specificity of bip. *J Biol Chem.* 1999;274:29850–29857.
26. Brodsky JL, Werner ED, Dubas ME, Goeckeler JL, Kruse KB, McCracken AA. The requirement for molecular chaperones during endoplasmic reticulum-associated protein degradation demonstrates that protein export and import are mechanistically distinct. *J Biol Chem.* 1999;274:3453–3460.
27. Meerovitch K, Wing S, Goltzman D. Proparathyroid hormone-related protein is associated with the chaperone protein BiP and undergoes proteasome-mediated degradation. *J Biol Chem.* 1998;273:21025–21030.
28. Katayama T, Imaizumi K, Sato N, et al. Presenilin-1 mutations downregulate the signalling pathway of the unfolded-protein response. *Nat Cell Biol.* 1999;1:479–485.
29. Yu Z, Luo H, Fu W, Mattson MP. The endoplasmic reticulum stress-responsive protein GRP78 protects neurons against excitotoxicity and apoptosis: suppression of oxidative stress and stabilization of calcium homeostasis. *Exp Neurol.* 1999;155:302–314.
30. Rao RV, Peel A, Logvinova A, et al. Coupling endoplasmic reticulum stress to the cell death program: role of the ER chaperone GRP78. *FEBS Lett.* 2002;514:122–128.
31. Reddy RK, Mao C, Baumeister P, Austin RC, Kaufman RJ, Lee AS. Endoplasmic reticulum chaperone protein GRP78 protects cells from apoptosis induced by topoisomerase inhibitors: role of ATP binding site in suppression of caspase-7 activation. *J Biol Chem.* 2003;278:20915–20924.
32. Kudo T, Kanemoto S, Hara H, et al. A molecular chaperone inducer protects neurons from ER stress. *Cell Death Differ.* 2008;15:364–375.
33. Krishnamoorthy RR, Agarwal P, Prasanna G, et al. Characterization of a transformed rat retinal ganglion cell line. *Brain Res Mol Brain Res.* 2001;86:1–12.
34. Chen D, Padiernos E, Ding F, Lossos IS, Lopez CD. Apoptosis-stimulating protein of p53-2 (ASPP2/53BP2L) is an E2F target gene. *Cell Death Differ.* 2005;12:358–368.
35. Jiang Y, Ahn EY, Ryu SH, et al. Cytotoxicity of psammaplin A from a two-sponge association may correlate with the inhibition of DNA replication. *BMC Cancer.* 2004;4:70.
36. Feng G, Mellor RH, Bernstein M, et al. Imaging neuronal subsets in transgenic mice expressing multiple spectral variants of GFP. *Neuron.* 2000;28:41–51.
37. Iwawaki T, Akai R, Kohno K, Miura M. A transgenic mouse model for monitoring endoplasmic reticulum stress. *Nat Med.* 2004;10:98–102.

38. Siliprandi R, Canella R, Carmignoto G, et al. N-methyl-D-aspartate-induced neurotoxicity in the adult rat retina. *Vis Neurosci.* 1992; 8:567–573.
39. Jeon CJ, Strettoi E, Masland RH. The major cell populations of the mouse retina. *J Neurosci.* 1998;18:8936–8946.
40. Onozuka T, Sawamura D, Goto M, Yokota K, Shimizu H. Possible role of endoplasmic reticulum stress in the pathogenesis of Darier's disease. *J Dermatol Sci.* 2006;41:217–220.
41. Weil M, Jacobson MD, Coles HS, et al. Constitutive expression of the machinery for programmed cell death. *J Cell Biol.* 1996;133: 1053–1059.
42. Taylor J, Gatchalian CL, Keen G, Rubin LL. Apoptosis in cerebellar granule neurones: involvement of interleukin-1 beta converting enzyme-like proteases. *J Neurochem.* 1997;68:1598–1605.
43. Inokuchi Y, Shimazawa M, Nakajima Y, Suemori S, Mishima S, Hara H. Brazilian green propolis protects against retinal damage in vitro and in vivo. *Evid Based Complement Alternat Med.* 2006;3:71–77.
44. Chidlow G, Wood JP, Manavis J, Osborne NN, Casson RJ. Expression of osteopontin in the rat retina: effects of excitotoxic and ischemic injuries. *Invest Ophthalmol Vis Sci.* 2008;49:762–771.
45. Sucher NJ, Lipton SA, Dreyer EB. Molecular basis of glutamate toxicity in retinal ganglion cells. *Vision Res.* 1997;37:3483–3493.
46. Henneberry RC, Novelli A, Cox JA, Lysko PG. Neurotoxicity at the N-methyl-D-aspartate receptor in energy-compromised neurons. An hypothesis for cell death in aging and disease. *Ann NY Acad Sci.* 1989;568:225–233.
47. Uehara T, Nakamura T, Yao D, et al. S-nitrosylated protein-disulphide isomerase links protein misfolding to neurodegeneration. *Nature.* 2006;441:513–517.
48. Wang XZ, Lawson B, Brewer JW, et al. Signals from the stressed endoplasmic reticulum induce C/EBP-homologous protein (CHOP/GADD153). *Mol Cell Biol.* 1996;16:4273–4280.
49. Ubeda M, Habener JF. CHOP gene expression in response to endoplasmic-reticular stress requires NFY interaction with different domains of a conserved DNA-binding element. *Nucleic Acids Res.* 2000;28:4987–4997.
50. Foti DM, Welihinda A, Kaufman RJ, Lee AS. Conservation and divergence of the yeast and mammalian unfolded protein response. Activation of specific mammalian endoplasmic reticulum stress element of the grp78/BiP promoter by yeast Hac1. *J Biol Chem.* 1999;274:30402–30409.